

---

Unterschrift E. Widmann



**TECHNISCHE  
UNIVERSITÄT  
WIEN**

DIPLOMARBEIT

**Design and Implementation of New Optics  
for the Atomic Hydrogen Beam of  
ASACUSA's Antihydrogen Hyperfine  
Spectroscopy Experiment**

Ausgeführt an der

Fakultät für Physik  
der Technischen Universität Wien

in Zusammenarbeit mit dem

Stefan Meyer Institut für Subatomare Physik  
der Österreichischen Akademie der Wissenschaften

unter der Anleitung von

Hon.-Prof. Dipl.-Phys. Dr. Eberhard Widmann

und

Dipl.-Ing. Dr. Martin C. Simon

durch

**Markus Wiesinger, BSc**  
Lampersdorf 3, 4133 Niederkappel.

14. Februar 2017

Datum

---

Unterschrift M. Wiesinger



## Abstract

The ASACUSA (Atomic Spectroscopy And Collisions Using Slow Antiprotons) collaboration at CERN will perform an experiment using Rabi's magnetic resonance method to measure the frequencies of ground state hyperfine transitions of antihydrogen. Since antihydrogen is the CPT symmetric partner of hydrogen and the frequency of these transitions in hydrogen are very well known, such measurements will provide a very sensitive test of CPT symmetry.

To prepare and characterize the spectroscopy apparatus for measurements with antihydrogen atoms, measurements with hydrogen atoms are performed. A beam of atomic hydrogen is used instead of the ASACUSA antihydrogen source, and a quadrupole mass spectrometer instead of an annihilation detector. A hyperfine spectroscopy apparatus (consisting of a cavity tuned to measure one of the two possible transitions, the  $\sigma$ -transition, and a superconducting sextupole magnet) has already been commissioned and is currently in operation at the ASACUSA antihydrogen hyperfine structure experiment at CERN.

In this work a second cavity is prepared, which enables simultaneous measurement of the two possible transitions, the  $\sigma$ - and  $\pi$ -transition. For operation with hydrogen the superconducting sextupole magnet is replaced by permanent sextupole magnets, which are built and characterized in the course of this work. The velocity and state selection properties of a sextupole doublet are simulated and measured. Numerical simulations of trajectories of hydrogen atoms in the spectroscopy apparatus are performed to obtain a quantitative understanding of the beam transport. These simulations lead to a new beam optics, based on ring apertures, which is implemented and tested. Finally, the  $\sigma$  and  $\pi$  hyperfine transitions of ground state hydrogen are measured with the spectroscopy apparatus in earth's magnetic field.



## Zusammenfassung

Die ASACUSA (Atomic Spectroscopy And Collisions Using Slow Antiprotons) Kollaboration am CERN wird ein Experiment unter Nutzung der Magnetresonanz-Methode von I. I. Rabi durchführen um die Frequenzen der Hyperfeinstruktur-Übergänge des Grundzustands von Antiwasserstoff zu vermessen. Da Antiwasserstoff der CPT-symmetrische Partner von Wasserstoff ist, und die Frequenzen dieser Übergänge in Wasserstoff sehr gut bekannt sind, stellen solche Messungen einen sehr empfindlichen Test der CPT Symmetrie dar.

Um den Spektroskopieapparat für den Betrieb mit Antiwasserstoffatomen vorzubereiten werden Messungen mit Wasserstoffatomen durchgeführt. Es wird ein Strahl von atomarem Wasserstoff anstelle der ASACUSA Antiwasserstoffquelle und ein Quadrupol-Massenspektrometer anstelle des Anihilations-Detektors verwendet. Ein Spektrometer (bestehend aus einer Kavität um einen der beiden möglichen Übergänge, den sogenannten  $\sigma$ -Übergang, zu messen und einem supraleitenden Sextupolmagneten) wurde bereits gebaut und charakterisiert und ist derzeit im Einsatz am ASACUSA Antiwasserstoff-Hyperfeinstruktur Experiment am CERN.

In dieser Arbeit wird eine zweite Kavität vorbereitet, die eine gleichzeitige Messung beider möglicher Übergänge (der  $\sigma$ - und  $\pi$ -Übergänge) erlaubt. Für den Betrieb mit Wasserstoff wird der supraleitende Sextupolmagnet durch permanente Sextupolmagnete ersetzt, die im Zuge dieser Arbeit gebaut und charakterisiert werden. Die Geschwindigkeits- und Zustandssektion eines Duplets aus Sextupolmagneten wird simuliert und vermessen. Numerische Simulationen zu den Trajektorien der Wasserstoffatome in dem Spektroskopieapparat werden durchgeführt, um ein quantitatives Verständnis des Strahltransports zu erhalten. Diese Simulationen führen zu einer neuen Strahloptik, basierend auf Ringblenden, die implementiert und getestet werden. Schließlich werden die  $\sigma$  und  $\pi$  Hyperfein-Übergänge des Grundzustands von Wasserstoff mit dem Spektroskopieapparat im Erdmagnetfeld vermessen.



## Acknowledgements

Zuallererst möchte ich meinen Eltern Edith und Ewald Wiesinger danken, denn ohne ihre ständige Unterstützung wäre weder mein Physikstudium noch diese Arbeit möglich gewesen. Vielen Dank!

Bedanken möchte ich mich auch bei Eberhard Widmann, der diese Arbeit betreut hat und mir die Gelegenheit gegeben hat an diesem spannenden Experiment mitzuarbeiten. Weiters gebührt ihm Dank für die Finanzierung meines Aufenthalts am Experiment in Genf.

Ich möchte mich auch bei Martin Simon bedanken, der diese Arbeit mitbetreut hat und mir spannende Einblicke in die experimentelle Physik ermöglicht hat. Ich danke ihm auch für die zahlreichen Diskussionen, die wir über die Physik geführt haben.

Bei den Doktorandinnen und Doktoranden am SMI möchte ich mich gerne für die tolle und kollegiale Atmosphäre bedanken. Es war mir eine Freude mit euch zu arbeiten!

Abschließend möchte ich mich bei all jenen Kolleginnen und Kollegen bedanken, die mich in Wien und in Zürich im Studium begleitet haben. Eure Beiträge haben das Studium erst so richtig spannend gemacht.



# Contents

<b>Abstract</b>	<b>iii</b>
<b>Zusammenfassung</b>	<b>v</b>
<b>1 Introduction</b>	<b>1</b>
<b>2 The Spectrum of the Hydrogen Atom</b>	<b>3</b>
2.1 Zeeman Effect . . . . .	6
<b>3 The Hydrogen Beam Experiment</b>	<b>11</b>
3.1 Rabi's Resonance Method . . . . .	11
3.2 Resonance Method of the Hydrogen Beam Experiment . . . . .	13
3.2.1 Hyperfine Transitions in Ground-state Hydrogen . . . . .	13
3.3 Hydrogen Source . . . . .	14
3.4 Alignment Laser and Photo Diode . . . . .	16
3.5 Velocity Selection and Polarization . . . . .	16
3.6 Chopper and Lock-in Amplifier . . . . .	17
3.7 Cavity . . . . .	18
3.8 Analysis Magnets . . . . .	19
3.9 Ring Aperture . . . . .	19
3.10 Detector . . . . .	19
3.11 Setup Configurations of the Hydrogen Beam Experiment . . . . .	20
3.11.1 Configuration 1 . . . . .	20
3.11.2 Configuration 2.1 "Permanent Magnets" . . . . .	20
3.11.3 Configuration 2.2 "Short Setup" . . . . .	21
3.11.4 Configuration 2.3 "Ring Aperture" . . . . .	21
<b>4 Magnetic Field Measurement of Analysis Sextupole Magnets</b>	<b>23</b>
4.1 Magnetic Field of an Ideal Sextupole . . . . .	23
4.2 SMI Sextupole Magnets . . . . .	23
4.3 Measurement Device . . . . .	25
4.4 Data Acquisition . . . . .	26
4.5 Field Reconstruction . . . . .	27
4.6 Analysis Method . . . . .	30
4.7 Comparison of Magnet Configurations . . . . .	32
4.8 Results . . . . .	34
<b>5 Velocity Selection of Polarizing Sextupoles</b>	<b>37</b>
5.1 Setup . . . . .	37
5.2 Method . . . . .	37
5.3 Analysis . . . . .	39
5.3.1 Laser Phase . . . . .	39

5.3.2	Beam Phase . . . . .	40
5.4	Result . . . . .	45
<b>6</b>	<b>Trajectory Simulations</b>	<b>47</b>
6.1	Force on Hydrogen Atoms . . . . .	47
6.2	Equations of Motion . . . . .	48
6.3	Numerical Algorithm . . . . .	50
6.4	Velocity Selection of a Sextupole Doublet . . . . .	51
6.5	Setup Configurations 2.1 and 2.2 . . . . .	53
6.6	Principle of New Beam Optics . . . . .	55
6.7	Setup Configuration 2.3 . . . . .	56
6.8	Summary of the Trajectory Simulations . . . . .	58
<b>7</b>	<b>Resonance Measurements</b>	<b>59</b>
7.1	Line Shape . . . . .	59
7.2	Measurement Method . . . . .	61
7.3	Analysis of $\pi$ - and $\sigma$ -Resonances in Earths Magnetic Field . .	62
7.3.1	Configuration 2.1 "Permanent Magnets" . . . . .	62
7.3.2	Configuration 2.3 "Ring Aperture" . . . . .	64
7.3.3	Comparison of Beam Rate and Total Count Rate . . .	64
7.4	Comparison with Simulation . . . . .	70
7.5	Comparison with Time of Flight Velocity Measurements . . .	72
7.6	Result . . . . .	73
<b>8</b>	<b>Conclusion</b>	<b>75</b>
<b>9</b>	<b>Appendix A: Physical Constants and Symbol Definitions</b>	<b>77</b>
	<b>References</b>	<b>79</b>

# 1 Introduction

In a process called pair production, matter can be created from the energy of photons or the kinetic energy of colliding particles. It is called pair production because in such events it is observed that for every matter particle created, there is also created an antimatter particle. Fundamental properties of matter and antimatter particles are either equal or opposite in sign, such that quantities as charge are conserved in these reactions. This matter antimatter symmetry is also included in the model that best describes the interaction of elementary particles – the Standard Model.

According to the Big Bang theory, at the origin of the universe there was a very high energy state. From this energy all the particles in the universe were created as the universe expanded and cooled. Applying the above rules, matter and antimatter should have been created in equal amounts. However, astronomical observations carried out to count the number of matter and antimatter particles in the universe show that our universe consists almost entirely of matter. This matter antimatter asymmetry in the universe is one of the important unresolved questions in physics.

In the Standard Model, the *CPT* symmetry is conserved. The *CPT* theorem states that processes in nature are invariant under simultaneous transformations of charge conjugation *C*, parity operation *P* and time reversal *T*. Therefore, properties of matter atoms and antimatter atoms like mass, spin, lifetime and their energy spectrum should be the same, while their charge and magnetic moments should be opposite. Several beyond the Standard Model theories, e.g. [1, 2], incorporate a violation of the *CPT* symmetry. It could help to explain the observed matter antimatter asymmetry.

To test the *CPT* symmetry, properties of particles and antiparticles have to be compared very precisely. Recent comparisons of mass over charge ratio [3] and magnetic moment [4] of single antiparticles have revealed no *CPT* violation. Antihydrogen is the simplest two particle system consisting entirely of antimatter. Furthermore, some properties of the hydrogen atom, such as the frequency of the 1s-2s transition [5] or the frequency of the zero field hyperfine splitting [6], are one of the most precisely known quantities in physics. For that reason, the comparison of the hydrogen atom with the antihydrogen atom will enable precise tests of the *CPT* symmetry.

Antihydrogen was first produced at CERN in 1996 by the PS210 experiment [7]. However, only 9 antihydrogen atoms were detected that travelled at velocities close to the speed of light. After the antiproton decelerator [8] has been installed at CERN, the first cold antihydrogen was produced in 2002 by trapping large numbers of antiprotons and mixing them with positrons [9,10]. The neutral antihydrogen however escaped from the traps and annihilated. The first trapping of antihydrogen was achieved by the ALPHA collaboration in 2010 [11]. At the moment several experiments are using the slow antiprotons provided by the antiproton decelerator to produce and trap cold

antihydrogen for experiments [11, 12].

The ACACUSA (Atomic Spectroscopy And Collisions Using Slow Antiprotons) collaboration intends to measure the frequencies of the ground state hyperfine transitions in antihydrogen [13–15]. Antiprotons are trapped within a cusp trap and mixed with positrons. A slow beam of polarized antihydrogen atoms emerges from the cusp trap [16, 17]. This beam is sent to a spectroscopy apparatus using the principle of Rabi’s resonance method [18] to measure the transition frequencies between the different energy levels of ground state antihydrogen.

The spectroscopy apparatus for antihydrogen [19] consists of a microwave cavity, an analysing sextupole magnet and an annihilation detector. At the right frequency the microwave cavity [20] drives the transition between the hyperfine levels. This leads to a flip of the positron spin. The superconducting sextupole magnet defocusses those antihydrogen atoms for which the transition occurred, while otherwise they get focussed onto the annihilation detector. To discriminate the annihilation signal of antihydrogen from background two layers of hodoscope bars around a central BGO detector are used, which enable vertex reconstruction [21, 22].

To prepare and characterize the spectroscopy apparatus for measurements with antihydrogen atoms, measurements with hydrogen atoms are performed [23]. A beam of atomic hydrogen [24] is used instead of the ASACUSA antihydrogen source, and a quadrupole mass spectrometer is used instead of the annihilation detector. A hyperfine spectroscopy apparatus (consisting of a cavity tuned to measure one of the two possible transitions, the  $\sigma$ -transition, and a superconducting sextupole magnet) has already been commissioned and is currently in operation at the ASACUSA antihydrogen hyperfine structure experiment [25, 26].

In the course of this work a second spectroscopy apparatus making use of a cavity which enables simultaneous measurements of the two possible transitions, the  $\sigma$ - and  $\pi$ -transition, is prepared. The experimental setup is described in chapter 3 after a short summary of the spectrum of the hydrogen atom in the next chapter. For operation with hydrogen the superconducting sextupole magnet is replaced by permanent sextupole magnets, which are built at the SMI<sup>1</sup> and are characterized in chapter 4 of this work. In chapter 5 the velocity and state selection properties of a doublet of permanent sextupole magnets are analyzed. Numerical simulations of trajectories of hydrogen atoms in the spectroscopy apparatus are reported in chapter 6. Finally, in chapter 7, a measurement of the  $\sigma$  and  $\pi$  hyperfine transitions of ground state hydrogen with the spectroscopy apparatus in earth’s magnetic field is presented.

---

<sup>1</sup>Stefan Meyer Institute for Subatomic Physics, Vienna, Austria.

## 2 The Spectrum of the Hydrogen Atom

Hydrogen is the simplest atom, consisting only of one proton surrounded by one electron. At first glance the spectrum of the hydrogen atom is very simple as well. However, the details of the spectrum reveal the influence of many interactions between the fundamental properties of the proton and the electron. Because of this, the hydrogen atom has been crucial to the understanding of quantum mechanics and quantum electrodynamics. And it will continue to be an interesting test object for the open questions in physics, especially in view of the recent progress in antihydrogen research.

The simplest quantum mechanical description of the hydrogen atom, taking into account only the Coulomb interaction of the electrical charge of the proton and the electrical charge of the electron in a non-relativistic way, is the Schrödinger model [27, 28]:

$$\left[ \frac{\vec{p}^2}{2m} - \frac{e^2}{4\pi\epsilon_0 r} \right] \psi = E_n \psi \quad (1)$$

where  $\psi$  is the scalar wave function,  $E_n$  the eigen energy and  $\vec{p}$  the momentum of the electron. The other symbols and quantities of the above and the following equations are defined in Appendix A. As a result the energies of the eigenstates depend only on the principal quantum number  $n$ :

$$E_n = -\frac{me^4}{2(4\pi\epsilon_0)^2 \hbar^2} \cdot \frac{1}{n^2} = -mc^2 \frac{\alpha^2}{2} \cdot \frac{1}{n^2} = -Ry \cdot \frac{1}{n^2}. \quad (2)$$

Dirac succeeded in giving the Schrödinger equation a Lorentz invariant form. Thereby relativistic effects<sup>2</sup> are taken into account, which naturally leads to a description of spin and antimatter [29, 30]. The Dirac equation reads

$$\left( c\vec{\alpha} \cdot \vec{p} + \beta mc^2 - \frac{e^2}{4\pi\epsilon_0 r} \right) \Psi = E_{n,j} \Psi \quad (3)$$

where  $\Psi$  is now a 4-component spinor wave function. As a result the energies of the eigenstates depend also on the total angular momentum quantum number  $j = l \pm \frac{1}{2}$ :

$$E_{n,j} = mc^2 \left( \left( 1 + \alpha^2 \left( n - j - \frac{1}{2} + \sqrt{\left( j + \frac{1}{2} \right)^2 - \alpha^2} \right)^{-2} \right)^{-\frac{1}{2}} - 1 \right) \quad (4)$$

$$\approx mc^2 \left( -\frac{\alpha^2}{2n^2} + \frac{\alpha^4(6j+3-8n)}{8(2j+1)n^4} + \dots \right) \quad (5)$$

This splitting of energy eigenstates is called fine structure of the hydrogen atom because the correction due to  $j$  is small. Note that eigenstates with

different orbital angular momentum  $l$  but the same total angular quantum number  $j$  are still degenerate in this model.

Taking into account quantum fluctuations of the electron field and quantum fluctuations of the photon field described by the theory of quantum electrodynamics [31, 32] there is a further contribution to the energy of the eigenstates. The shift depends on the orbital angular momentum  $l$  such that the energy of states with different  $n, j$  and  $l$  is different. This shift in energy of the eigenstates is called Lamb shift and its magnitude is to first order:

$$E_{n,l,j} = E_{n,j} + mc^2 \frac{\alpha^2}{2} \frac{8\alpha^3}{3\pi} \frac{1}{n^3} \left( \log \left( \frac{m_e c^2}{2(E - E_0)_{\text{avg}}} \right) + \frac{5}{6} - \frac{1}{5} \right), \quad l = 0 \quad (11)$$

$$= E_{n,j} + mc^2 \frac{\alpha^2}{2} \frac{\alpha^3}{2\pi} \frac{1}{n^3} \left( \frac{1}{(l + 1/2)(l + 1)} \right), \quad l \neq 0, j = l + 1/2 \quad (12)$$

$$= E_{n,j} + mc^2 \frac{\alpha^2}{2} \frac{\alpha^3}{2\pi} \frac{1}{n^3} \left( -\frac{1}{l(l + 1/2)} \right), \quad l \neq 0, j = l - 1/2 \quad (13)$$

See also chapter 8 in the lecture notes of Dyson [33].

Taking into account the interaction of the magnetic moment of the proton with the magnetic moment of the electron using the hamiltonian

$$H = -\frac{2\mu_0}{3} \vec{\mu}_e \cdot \vec{\mu}_p \delta(\vec{x}_e - \vec{x}_p) - \frac{\mu_0}{4\pi} \frac{1}{r^3} \left[ 3 \frac{\vec{\mu}_1 \cdot \vec{r}}{r} \frac{\vec{\mu}_2 \cdot \vec{r}}{r} - \vec{\mu}_1 \cdot \vec{\mu}_2 \right] \quad (14)$$

there is an even smaller splitting of the energy of the eigenstates. This splitting is the so called hyperfine splitting. The first term in equation 14 is

<sup>2</sup>In the non-relativistic limit the hamiltonian of the Dirac equation can be expressed as

$$\left[ \frac{\vec{p}^2}{2m} - \frac{\vec{p}^2 \vec{p}^2}{8m^3 c^2} + \frac{\hbar^2}{8m^2 c^2} (\vec{\nabla}^2 V(r)) + \frac{1}{2m^2 c^2} \frac{1}{r} \frac{dV}{dr} \vec{L} \cdot \vec{S} + V(r) \right] \psi = E_{n,l} \psi \quad (6)$$

with  $V(r) = -\frac{Ze^2}{4\pi\epsilon_0 r}$ . The three terms are the relativistic mass increase

$$E_{n,l} = E_n \left[ 1 - \frac{\alpha^2 Z^2}{n^2} \left( \frac{3}{4} - \frac{n}{l + 1/2} \right) \right], \quad (7)$$

the Darwin term (a result of the zitterbewegung of the electron)

$$E = 4Z^4 mc^2 \alpha^4 \delta_{l0}, \quad (8)$$

and the spin orbit interaction

$$E_{n,l,j} = E_n \left[ 1 - \frac{1}{2} \frac{Z^2 \alpha^2}{nl(l + 1/2)(l + 1)} [j(j + 1) - l(l + 1) - s(s + 1)] \right]. \quad (9)$$

In total the energy shift according to the hamiltonian (equation 6) is

$$E_{n,j} = E_n \left[ 1 - \frac{\alpha^2 Z^2}{n^2} \left( \frac{3}{4} - \frac{n}{j + 1/2} \right) \right] \quad (10)$$

which agrees with the expansion of equation 4.

the Fermi contact interaction [34] and for the  $l = 0$  states of the hydrogen atom the contribution to the energy of the eigenstates is:

$$E_{n,l,j,F} = E_{n,l,j} - \frac{2\mu_0}{3} g_e g_p \frac{m_e}{m_p} \mu_B^2 \frac{\hat{s}_e \cdot \hat{s}_p}{\hbar^2} |\Psi_n(0)|^2. \quad (15)$$

Because both electron and proton are spin- $\frac{1}{2}$  particles and

$$\hat{s}_e \cdot \hat{s}_p = \frac{\hbar^2}{2} [(s_e + s_p)(s_e + s_p + 1) - s_e(s_e + 1) - s_p(s_p + 1)] = \begin{cases} +\frac{1}{4}\hbar^2 \\ -\frac{3}{4}\hbar^2 \end{cases} \quad (16)$$

there are (for  $l = 0$ ) two states with energy difference

$$-\frac{2\mu_0}{3} g_e g_p \frac{m_e}{m_p} \mu_B^2 |\Psi_n(0)|^2. \quad (17)$$

Expressing  $\mu_B$  as a function of  $\alpha$  and using  $|\Psi_n(0)|^2 = \frac{m^3 c^3 \alpha^3}{\pi \hbar^3}$ , the hyperfine splitting of the ground state of the hydrogen atom therefore becomes

$$h\nu_0 = \Delta E_{\text{HFS}} = -\frac{2}{3} \left( \frac{m^3}{m_e^3} \right) g_e g_p m_e c^2 \alpha^4 \frac{m_e}{m_p}. \quad (18)$$

where  $m = m_e m_p / (m_e + m_p)$  is the reduced mass,  $m_e$  the electron mass, and  $m_p$  the proton mass.

Even smaller contributions such as the magnetic size of the proton (Zemach correction) and polarizability of the proton have to be taken into account if the theoretical values are compared with the extremely precise measurements of  $\nu_0$  utilizing the hydrogen maser [6].

To summarize the above, many different effects influence the spectrum of such a simple system as the hydrogen atom. Interestingly the order of magnitude of these influences can be described in terms of the fine structure constant:

- The mass energy of the electron:  $m_e c^2$ .
- The binding energy due to the electromagnetic interaction:  $m_e c^2 \alpha^2$ .
- The magnitude of relativistic corrections:  $m_e c^2 \alpha^4$ .
- The magnitude of corrections due to quantum field theory:  $m_e c^2 \alpha^5$ .
- And the magnitude according to spin spin interaction:  $m_e c^2 \alpha^4 \frac{m_e}{m_p}$ .

## 2.1 Zeeman Effect

Above only the interaction of the magnetic moment of the electron with the magnetic moment of the proton was discussed. In the presence of an external magnetic field  $\vec{B}$  the magnetic moments of electron and proton also interact with the external field. As one can read for example in chapter 12 in [35], this can be expressed using the hamiltonian

$$H = -\frac{2\mu_0}{3}\vec{\mu}_e \cdot \vec{\mu}_p |\Psi_1(0)|^2 - \vec{\mu}_e \cdot \vec{B} - \vec{\mu}_p \cdot \vec{B}. \quad (19)$$

Using the positive constant  $A = -\frac{1}{4}\frac{2\mu_0}{3}g_e g_p \frac{m_e}{m_p} \mu_B^2 \frac{m^3 c^3 \alpha^3}{\pi \hbar^3}$ , which describes the coupling of the two spins, this can also be expressed in terms of the spin operators

$$H = A \frac{4}{\hbar^2} \hat{s}_e \cdot \hat{s}_p - g_e \mu_B \frac{1}{\hbar} \hat{s}_e \cdot \vec{B} - g_p \frac{m_e}{m_p} \mu_B \frac{1}{\hbar} \hat{s}_p \cdot \vec{B}. \quad (20)$$

Using the following complete basis

$$|s_e^z, s_p^z\rangle = \left| \frac{1}{2}, \frac{1}{2} \right\rangle, \left| \frac{1}{2}, -\frac{1}{2} \right\rangle, \left| -\frac{1}{2}, \frac{1}{2} \right\rangle, \left| -\frac{1}{2}, -\frac{1}{2} \right\rangle \quad (21)$$

and  $\vec{B} = B\vec{e}_z$  the hamiltonian becomes

$$H = \begin{pmatrix} \mu B + A & 0 & 0 & 0 \\ 0 & \mu' B - A & 2A & 0 \\ 0 & 2A & -\mu' B - A & 0 \\ 0 & 0 & 0 & -\mu B + A \end{pmatrix} \quad (22)$$

with the positive constants

$$\mu = -\frac{1}{2}(g_e \mu_B + g_p \frac{m_e}{m_p} \mu_B) \quad (23)$$

and

$$\mu' = -\frac{1}{2}(g_e \mu_B - g_p \frac{m_e}{m_p} \mu_B). \quad (24)$$

To obtain the eigenstates and their energies the eigenvalue problem

$$H |\Psi\rangle = E \mathbb{1} |\Psi\rangle \quad (25)$$

must be solved. By expanding  $|\Psi\rangle$  using the above basis<sup>3</sup>

$$|\Psi\rangle = \mathbb{1} |\Psi\rangle = \sum_{n=1}^4 |n\rangle \langle n|\Psi\rangle = \sum_{n=1}^4 a_n |n\rangle \quad (28)$$

---

<sup>3</sup>the base states  $|n\rangle$  are numbered by roman numerals

$$|I\rangle = \left| \frac{1}{2}, \frac{1}{2} \right\rangle \quad |II\rangle = \left| \frac{1}{2}, -\frac{1}{2} \right\rangle \quad (26)$$

$$|III\rangle = \left| -\frac{1}{2}, \frac{1}{2} \right\rangle \quad |IV\rangle = \left| -\frac{1}{2}, -\frac{1}{2} \right\rangle \quad (27)$$

with the coefficients  $a_n$  one obtains the equations

$$Ea_1 = (A + \mu B)a_1 \quad (29)$$

$$Ea_2 = (-A + \mu' B)a_2 + 2Aa_3 \quad (30)$$

$$Ea_3 = (-A - \mu' B)a_3 + 2Aa_2 \quad (31)$$

$$Ea_4 = (A - \mu B)a_4 \quad (32)$$

The first and the last equation are independent of all others and the two solutions

$$E_1 = A + \mu B \quad \text{with} \quad a_1 = 1, \quad a_2 = a_3 = a_4 = 0 \quad (33)$$

$$E_3 = A - \mu B \quad \text{with} \quad a_1 = a_2 = a_3 = 0, \quad a_4 = 1 \quad (34)$$

are immediately found.

For the other two solutions equations 30 and 31 must be solved simultaneously. The energies obtained by solving are:

$$E_2 = -A + \sqrt{\mu'^2 B^2 + 4A^2} \quad (35)$$

$$E_4 = -A - \sqrt{\mu'^2 B^2 + 4A^2} \quad (36)$$

For the energy  $E_2$  the coefficients  $a_1 = 0$  and  $a_4 = 0$  and the ratio

$$\frac{a_2}{a_3} = \frac{E_2 + A + \mu' B}{2A} \quad (37)$$

$$= \sqrt{1 + \left(\frac{\mu' B}{2A}\right)^2} + \frac{\mu' B}{2A}. \quad (38)$$

Using the ansatz

$$a_2 = \cos \vartheta, \quad a_3 = \sin \vartheta \quad (39)$$

which satisfies

$$a_2^2 + a_3^2 = 1 \quad (40)$$

leads to the equation for the mixing angle

$$\vartheta = \arctan\left(\frac{1}{\sqrt{1 + x^2} + x}\right) \quad (41)$$

where  $x = B/B_C$  with  $B_C = 2A/\mu'$ . The eigenstate  $|2\rangle$  to the energy  $E_2$  becomes:

$$|2\rangle = \cos \vartheta \left| \frac{1}{2}, -\frac{1}{2} \right\rangle + \sin \vartheta \left| -\frac{1}{2}, \frac{1}{2} \right\rangle. \quad (42)$$

A similar ansatz for the energy  $E_4$

$$a_2 = -\sin \vartheta, \quad a_3 = \cos \vartheta \quad (43)$$

gives the eigenstate to energy  $E_4$

$$|4\rangle = -\sin\vartheta \left| \frac{1}{2}, -\frac{1}{2} \right\rangle + \cos\vartheta \left| -\frac{1}{2}, \frac{1}{2} \right\rangle \quad (44)$$

with the same mixing angle  $\vartheta$  as above.

To get the magnetic moment of the eigenstates the operator

$$\hat{\vec{\mu}} = g_e \mu_B \frac{1}{\hbar} \hat{s}_e + g_p \frac{m_e}{m_p} \mu_B \frac{1}{\hbar} \hat{s}_p \quad (45)$$

is applied to the eigenstates: For state  $|4\rangle$  as an example  $\mu_4$  is

$$\langle 4 | \hat{\vec{\mu}} | 4 \rangle = \left( -\sin\vartheta \left\langle \frac{1}{2}, -\frac{1}{2} \right| + \cos\vartheta \left\langle -\frac{1}{2}, \frac{1}{2} \right| \right) \left( g_e \mu_B \frac{1}{\hbar} \hat{s}_e + g_p \frac{m_e}{m_p} \mu_B \frac{1}{\hbar} \hat{s}_p \right) \quad (46)$$

$$\cdot \left( -\sin\vartheta \left| \frac{1}{2}, -\frac{1}{2} \right\rangle + \cos\vartheta \left| -\frac{1}{2}, \frac{1}{2} \right\rangle \right) \quad (47)$$

$$= -\frac{1}{2} \left( g_e \mu_B - g_p \frac{m_e}{m_p} \mu_B \right) \frac{B/B_C}{\sqrt{1 + (B/B_C)^2}} \vec{e}_z \quad (48)$$

and similarly for the other states.

For  $B = 0$  the energy difference between the degenerate states  $|1\rangle, |2\rangle$ , and  $|3\rangle$  and the state  $|4\rangle$  becomes  $4A$ . Therefore,  $A$  can be expressed in terms of the frequency of the hyperfine transition in zero magnetic field  $\nu_0$ :

$$A = \frac{1}{4} h \nu_0. \quad (49)$$

To summarize all the above, the ground state of the hydrogen atom actually consists of the following 4 eigenstates

$$|1\rangle = \left| \frac{1}{2}, \frac{1}{2} \right\rangle \quad (50)$$

$$|2\rangle = +\cos\vartheta \left| \frac{1}{2}, -\frac{1}{2} \right\rangle + \sin\vartheta \left| -\frac{1}{2}, \frac{1}{2} \right\rangle \quad (51)$$

$$|3\rangle = \left| -\frac{1}{2}, -\frac{1}{2} \right\rangle \quad (52)$$

$$|4\rangle = -\sin\vartheta \left| \frac{1}{2}, -\frac{1}{2} \right\rangle + \cos\vartheta \left| -\frac{1}{2}, \frac{1}{2} \right\rangle \quad (53)$$

with the eigen energies

$$E_1 = + \frac{h\nu_0}{4} - \frac{1}{2}(g_e\mu_B + g_p\frac{m_e}{m_p}\mu_B)B \quad (54)$$

$$E_2 = - \frac{h\nu_0}{4} + \frac{h\nu_0}{2}\sqrt{1 + (B/B_C)^2} \quad (55)$$

$$E_3 = + \frac{h\nu_0}{4} + \frac{1}{2}(g_e\mu_B + g_p\frac{m_e}{m_p}\mu_B)B \quad (56)$$

$$E_4 = - \frac{h\nu_0}{4} - \frac{h\nu_0}{2}\sqrt{1 + (B/B_C)^2}. \quad (57)$$

The magnetic momenta of the 4 eigenstates of hydrogen are:

$$\mu_1 = + \frac{1}{2}(g_e\mu_B + g_p\frac{m_e}{m_p}\mu_B) \quad (58)$$

$$\mu_2 = + \frac{1}{2}(g_e\mu_B - g_p\frac{m_e}{m_p}\mu_B)\frac{B/B_C}{\sqrt{1 + (B/B_C)^2}} \quad (59)$$

$$\mu_3 = - \frac{1}{2}(g_e\mu_B + g_p\frac{m_e}{m_p}\mu_B) \quad (60)$$

$$\mu_4 = - \frac{1}{2}(g_e\mu_B - g_p\frac{m_e}{m_p}\mu_B)\frac{B/B_C}{\sqrt{1 + (B/B_C)^2}} \quad (61)$$

with

$$\vartheta = \arctan\left(\frac{1}{\sqrt{1 + (B/B_C)^2} + B/B_C}\right) = \frac{1}{2}\arctan(B_C/B) \quad (62)$$

$$B_C = \frac{h\nu_0}{2\mu'} = \frac{h\nu_0}{-(g_e\mu_B - g_p\frac{m_e}{m_p}\mu_B)}. \quad (63)$$

The angle  $\vartheta$  describes the mixing of the base states  $|II\rangle$  and  $|III\rangle$  into the eigenstates  $|2\rangle$  and  $|4\rangle$ . For zero magnetic field the mixing angle is  $\vartheta = \frac{\pi}{4}$  (maximal mixing) and the eigenstates  $|2\rangle$  and  $|4\rangle$  become

$$|2\rangle = +\frac{1}{\sqrt{2}}|II\rangle + \frac{1}{\sqrt{2}}|III\rangle \quad (64)$$

$$|4\rangle = -\frac{1}{\sqrt{2}}|II\rangle + \frac{1}{\sqrt{2}}|III\rangle \quad (65)$$

For infinitely large magnetic fields the mixing angle is  $\vartheta = 0$  (minimal mixing) and the eigenstates become

$$|2\rangle = |II\rangle \quad (66)$$

$$|4\rangle = |III\rangle \quad (67)$$

At the characteristic magnetic field  $B_c$  the mixing angle is  $\vartheta = \frac{\pi}{8}$ , half its maximal value. The mixing changes from maximal to minimal mixing at the characteristic magnetic field.

The energies and magnetic momenta of the four eigenstates are shown in figure 1. For state  $|1\rangle$  and  $|3\rangle$  the energy depends linearly on the magnetic field. Therefore the magnetic moment is constant. States  $|2\rangle$  and  $|4\rangle$  are a mixture of base states. Because of that, the magnetic momenta of the states  $|2\rangle$  and  $|4\rangle$  vary with the magnetic field. They are zero for zero magnetic field and become  $\pm\mu'$  for large magnetic fields.

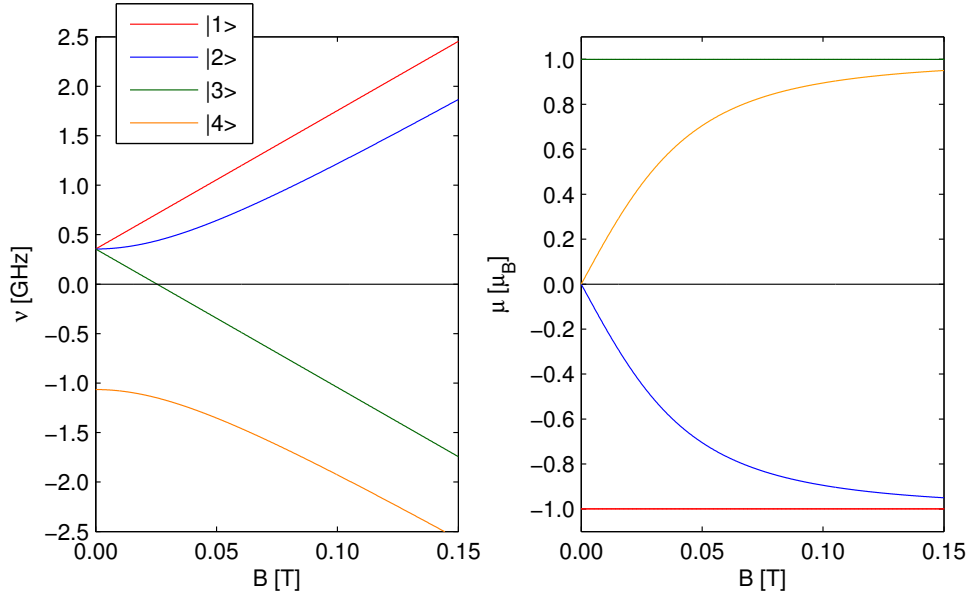


Figure 1: Energies (left) and magnetic momenta (right) of the four eigenstates of the ground state of hydrogen in dependence of the external magnetic field.

### 3 The Hydrogen Beam Experiment

The aim of the antihydrogen programme of the ASACUSA collaboration is the measurement of the hyperfine structure of antihydrogen in a beam. The first beam of antihydrogen atoms was produced by ASACUSA in 2012 [17]. Despite a production rate of several 1000 hydrogen atoms per cycle, the number of antihydrogen atoms that reach the detector as a beam currently is only  $\approx 1$  per cycle ( $\approx 20$  minutes). This rate is too small for calibration and testing purposes. For this reason, the hydrogen beam experiment was set up in order to prepare the spectroscopy apparatus for the hyperfine structure measurement.

Both, the antihydrogen experiment and the hydrogen beam experiment use the magnetic resonance technique of I. I. Rabi [18]. The antihydrogen spectroscopy apparatus is designed to receive a polarized beam of antihydrogen atoms. It consists of a cavity to induce transitions, a sextupole magnet to perform state selection, and an annihilation detector [19].

The different elements between the first configuration of the hydrogen beam experiment and the antihydrogen experiment are the source and the detector, which both need to be very different for hydrogen and antihydrogen. The common elements, which are the main part of the spectroscopy apparatus, are the strip line cavity and the superconducting sextupole magnet. In this first setup the constant magnetic field at the cavity is parallel to the oscillating field inside the cavity, therefore, only the  $\sigma$ -transition can be detected.

For the second configuration of the hydrogen beam experiment the superconducting sextupole magnet was not available, because it was in operation at the antihydrogen experiment. Therefore, permanent magnets were built at SMI to replace the superconducting sextupole magnet. The main purpose of the second configuration of the hydrogen beam experiment is the preparation of a second cavity where the constant magnetic field has components both parallel and orthogonal to the oscillating field, which enables the measurement of both,  $\sigma$ - and  $\pi$ -transitions.

A detailed description of the hydrogen beam experiment can be found in [19] and [26]. A short summary is provided below.

#### 3.1 Rabi's Resonance Method

The magnetic resonance method was introduced by Rabi in 1937 [36] and was subsequently used to measure the spin and the magnetic moment of several nuclei [18, 37].

The apparatus (see figure 2) consists of two magnets with inhomogeneous field (magnet A and magnet B) and a magnet with homogeneous field (magnet C) in between. The magnetic field is strong and points in the same direction from the start of magnet A to the end of magnet B. The gradient

in magnet A and magnet B is of opposite direction.

A beam of molecules is emitted from an oven (O). Because of their nuclear magnetic moment, the molecules are deflected in the inhomogeneous fields of magnet A and magnet B. The deflection is opposite in direction for the magnet A and magnet B such that the path of the molecules is s-shaped. The magnitude of the fields in magnet A and magnet B is such that the deflection cancels for molecules that pass the slit (S), and the beam arrives at the detector (D).

A magnetic moment with an angular momentum will precess in an external magnetic field with the Larmor frequency<sup>4</sup>  $\nu_L$ . The projection of the magnetic moment onto the magnetic field determines the magnitude of deflection. If the orientation of the magnetic moment is altered<sup>5</sup> by an oscillating field with frequency  $\nu$  in the region of the constant field of magnet C, the molecules are deflected differently and do not arrive at the detector (dashed lines).

The magnetic moment is only altered by the oscillating field if its frequency is close to the Larmor frequency. Therefore, the resonance can be observed as a drop in signal at the detector when  $\nu$  is close to  $\nu_L$ .

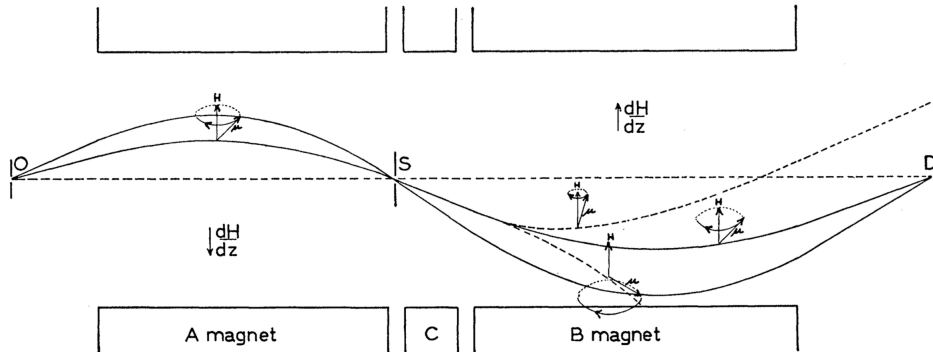


Figure 2: A schematic diagram of the experimental setup used by Rabi et al. to measure the nuclear magnetic moments of  ${}^6\text{Li}$ ,  ${}^7\text{Li}$  and  ${}^{19}\text{F}$ . From [18].

<sup>4</sup>The Larmor frequency is  $\nu_L = \gamma B$  with the gyromagnetic ratio  $\gamma$  defined by  $\vec{\mu} = \gamma \vec{L}$ . For an elementary particle  $\gamma = g_x q_x / (2m_x)$  with mass  $m_x$ , charge  $q_x$ , and Landé factor  $g_x$  of the particle.

<sup>5</sup>The classical magnetic moment can be altered continuously, while the magnetic moment of an elementary particle can jump between discrete states that depend on the spin projection. This quantum jump corresponds to a transition.

## 3.2 Resonance Method of the Hydrogen Beam Experiment

The hydrogen beam setup features a rotationally symmetric beam and deflecting magnet configuration<sup>6</sup>. A cylindrical coordinate system with the  $z$ -axis coaxial to the beam is chosen, where the radius  $r$  measures the distance to the beam axis. The arrangement is independent of  $\varphi$ .

The apparatus (schematically shown in figure 3) consists of two magnets with a sextupole field (A and B) and a section with a constant homogeneous field in between (C). In the area of the constant homogeneous field a cavity is installed, which enables the application of an oscillating field. The field gradient of the sextupole magnets increases linearly with the radius.

A beam of hydrogen atoms is emitted from the source (S). Because of their magnetic moment (see figure 1) the hydrogen atoms are deflected in radial direction. The deflection is larger for larger radii, such that all will be focussed at the same point downstream of the magnet if their magnetic moment and their velocity is the same. The deflection is either focussing or defocussing, depending on the sign of the magnetic moment.

Magnet A focusses the states with negative magnetic moment (thick lines) onto a focal point<sup>7</sup>. Magnet B focusses the diverging beam again onto the detector (D). Both magnets are arranged in such a way that the signal at the detector is a maximum. Only atomic states with negative magnetic moment will arrive at the detector, because atomic states with positive magnetic moment will be defocussed (thin lines).

If an oscillating field with frequency  $\nu$  is applied in addition to the constant homogeneous field in the area between the sextupole magnets (C), a transition to another atomic state may occur. If the final state of the transition has the opposite magnetic moment, the atom will be deflected by magnet B and will not arrive at the detector.

Transitions only occur if the frequency of the oscillating field is close to the transition frequency  $\nu_T = \Delta E/h$ . Therefore, the transition can be observed as a drop in signal at the detector when  $\nu$  is close to  $\nu_T$ .

### 3.2.1 Hyperfine Transitions in Ground-state Hydrogen

The eigenstates of the hydrogen atom in its ground state have been discussed in section 2.1. The ground state actually splits up in four states due to the hyperfine interaction, their energy (in frequency units) is shown in figure 4 as a function of the magnetic field.

---

<sup>6</sup>The rotationally symmetric configuration with sextupole magnets for deflection was introduced by D. R. Hamilton, a former student of I. I. Rabi.

<sup>7</sup>In figure 3 the focal point is displayed between magnet A and B. But any point downstream of magnet A is possible depending on the velocity of the atoms (smaller velocity atoms are deflected more and the focal point is closer to magnet A). If the focal point is chosen to be at infinity, there is a parallel beam between magnet A and B.

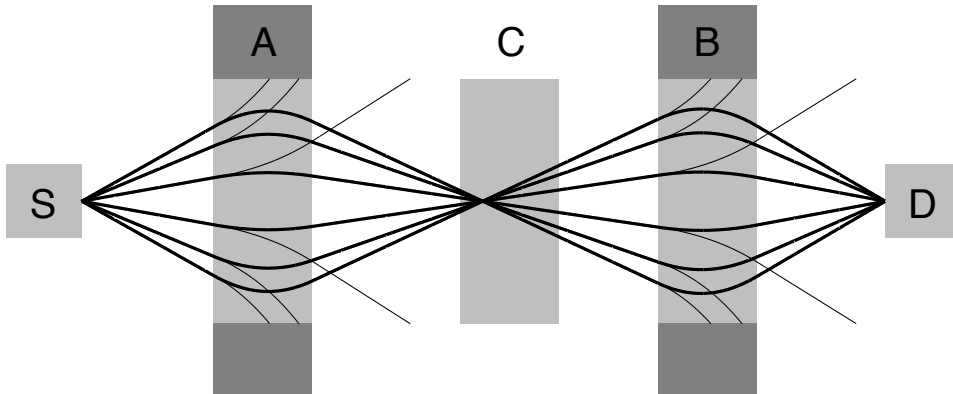


Figure 3: A schematic diagram of the experimental setup of the hydrogen beam experiment.

In the hydrogen beam experiment, transitions from states with negative magnetic moment (states  $|1\rangle$  and  $|2\rangle$ ) to states with positive magnetic moment (states  $|3\rangle$  and  $|4\rangle$ ) can be detected. An additional limitation is the frequency range of the cavity, which rules out transitions to state  $|3\rangle$ .

Therefore, two transitions can be measured by the hydrogen beam experiment: The  $\sigma$ -resonance is the transition from the state  $|2\rangle$  to the state  $|4\rangle$ . The  $\pi$ -resonance is the transition from state  $|1\rangle$  to state  $|4\rangle$ . See figure 4. Their transition frequencies are:

$$\nu_\sigma = \nu_0 \sqrt{1 + (B/B_C)^2} \quad (68)$$

$$\nu_\pi = \frac{\nu_0}{2} \left( 1 + \sqrt{1 + (B/B_C)^2} \right) - \frac{1}{2} \left( g_e \mu_B + g_p \frac{m_e}{m_p} \mu_B \right) \frac{B}{h} \quad (69)$$

For low magnetic fields the frequency of the  $\sigma$ -transition depends quadratically on the magnetic field. Therefore, influences of inhomogeneities of the magnetic field on the transition frequency are small. The frequency of the  $\pi$ -transition depends linearly on the magnetic field. Therefore, this transition is more sensitive to magnetic field inhomogeneities.

### 3.3 Hydrogen Source

To create atomic hydrogen, molecular hydrogen needs to be dissociated. In this experiment a radio frequency discharge tube is used for this purpose. A pyrex glass tube contains the hydrogen gas. It is encapsulated by a water cooled radio frequency antenna to couple the electromagnetic waves to the plasma. On one end molecular hydrogen is fed into the glass tube with constant mass flow rate. On the other end the pyrex glass tube narrows and forms a pipe with a diameter of 1 mm, where atomic hydrogen is extracted (figure 5).

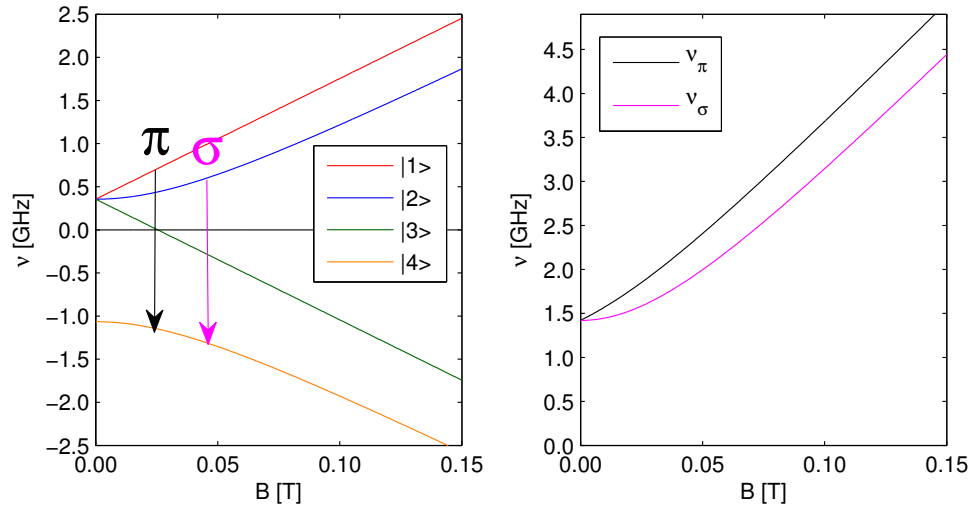
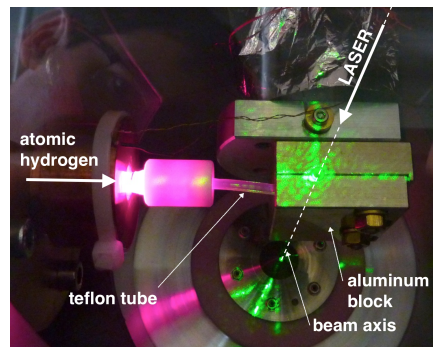


Figure 4: Breit Rabi diagram (left). Magnetic field dependence of the transition frequency for  $\sigma$ - and  $\pi$ -transitions (right).



(a) Pyrex tube with radio frequency antenna.



(b) Atomic hydrogen source assembly.

Figure 5: Atomic hydrogen source. Pyrex tube and radio frequency antenna (left) and full assembly (right).

The source is mounted transverse to the beam axis. A pipe of teflon with a 90° bend is used to transfer the atomic hydrogen from the source to the beam axis. At the bend the teflon pipe is encapsulated in an aluminum block, which is cooled to 20 K by a helium cryostat. The gas of atomic hydrogen enters the teflon pipe at room temperature, is cooled to  $\approx 20$  K through collisions with the wall of the cooled teflon tube, and exits the teflon tube as a beam of cold hydrogen atoms.

### 3.4 Alignment Laser and Photo Diode

A small hole, coaxial with the exit of the teflon tube, is drilled into the aluminum block of the source. This allows an alignment laser to be projected through this hole, such that the axis of the laser and the axis of the atomic beam of hydrogen are coaxially aligned.

The laser beam is introduced through a glass window in the source vacuum chamber. It travels through all subsequent components of the setup and is detected by a photo diode with a filter matched to the laser frequency. The laser beam is used for two purposes: Optical alignment of the beam line components, and determination of the amplitude and phase of the chopper opening (see section 3.6).

### 3.5 Velocity Selection and Polarization

For initial beam polarization and velocity selection a doublet of permanent sextupole magnets is used. Those are referred to as the CERN magnets, because they were built by the CERN normal conducting magnets laboratory. A detailed description of these magnets can be found in [38].

The CERN magnets are 65 mm long, with an aperture diameter of 10 mm and an integrated gradient<sup>8</sup> $G_s$  of 7435 T m<sup>-1</sup>. The field at the poles is 1.36 T. Both magnets are identical and mounted on a slide which enables the variation of the distance between the magnets from 16 mm to 116 mm. In the middle of the two magnets an aperture with a diameter of 3 mm is installed. This aperture can be exchanged and several diameters from 1 mm to 5 mm are available.

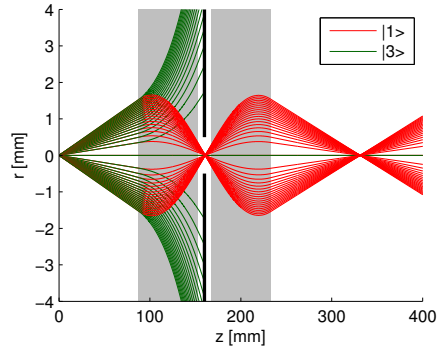
When the hydrogen atoms enter the first magnet, a force is exerted onto the hydrogen atoms by the gradient of the magnetic sextupole field. The force is directed either radially inwards or outwards, depending on the magnetic moment of the state of the hydrogen atom. For the states with negative magnetic moment the force is directed radially inwards and they are focussed onto the aperture, if the velocity matches. For states with positive magnetic moment the force is directed radially outwards. Such atoms are removed from the beam.

---

<sup>8</sup>The integrated gradient  $G_s = \int_{-\infty}^{\infty} g_s(z) dz$  is the integral of the parameter  $g_s$  which describes the strength of the sextupole field  $\vec{B} = (g_s xy, g_s x^2/2 - g_s y^2/2, 0)$ .



(a) CERN magnets assembly for velocity selection and polarization. The aperture has been removed for this image.



(b) Beam trajectories in the velocity selection area. The magnets are marked in grey. States  $|3\rangle$  are stopped by the aperture in black.

Figure 6: Velocity selection and polarization magnets. Assembly (left) and beam trajectories (right).

The aperture selects only the part of the beam that is focussed onto it. The second magnet focusses the beam again. Because the arrangement is symmetric, the second magnet ensures that the beam leaves the second magnet with the same divergence the beam entered the first magnet.

The distance of the focal point from the magnet depends on the velocity of the beam. Therefore, for different distances of the magnets different velocities are selected. In this way polarization and velocity selection of the beam is achieved simultaneously.

A measurement of the velocity selection of the assembly is described in chapter 5.

### 3.6 Chopper and Lock-in Amplifier

The beam is chopped by a tuning fork chopper (model Scitec CH-10) with a duty cycle of 50%. The tuning fork chopper consists of two blades which oscillate with a frequency of  $\approx 180$  Hz. As a result, the transmitted beam intensity varies in time as the positive half-wave of a sine<sup>9</sup>.

The detector readout is based on a lock-in amplification scheme [39] utilizing the chopper frequency. First the phase of the chopper signal is binned into 200 bins, where every phase bin corresponds to a time bin. Then the counts of the detector signal that occur in a given time bin are assigned to the corresponding phase bin. The counts are summed over a time period much larger than the oscillating period of the chopper. The result is a histogram of detector counts versus phase.

<sup>9</sup>This is only true under the condition that the beam size is larger than the chopper amplitude, which is satisfied in the used setup.

This histogram is used to reconstruct two parts of the signal: The constant part corresponds to the signal of a constant background and is called background rate. The time (phase) varying part corresponds to the signal of the chopped beam and is called beam rate. Figure 7 schematically shows a typical histogram of detector count rate versus chopper phase.

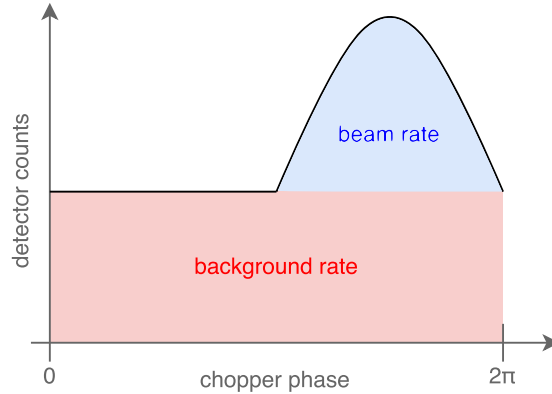
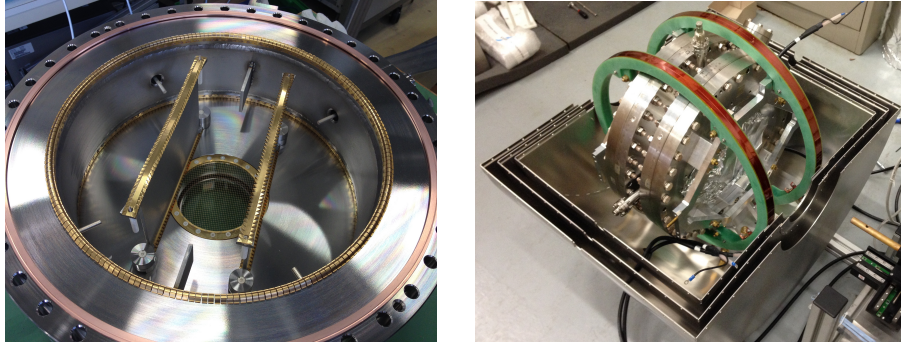


Figure 7: Schematic diagram of detector count rate versus chopper phase. The beam rate and background rate are indicated in blue and red, respectively.

### 3.7 Cavity

A microwave cavity (figure 8) tuned to the transition frequency of 1420 MHz is used to drive the transitions. A low Q factor allows the frequency to be scanned over a range of  $\approx 6$  MHz. The cavity features a special design making use of striplines (thin parallel plates of conductive material). This provides a homogeneous oscillating field at each cross section of the active volume of 100 mm diameter and 105.5 mm length. Four antennas equally spaced around the cylinder enable the coupling of the radio frequency to the cavity [20].

The radio frequency is supplied by a ZVB20 vector network analyzer and amplified by a radio frequency amplifier with an amplification factor of 52 dB. The amplified radio frequency signal is coupled to the cavity via a stub tuner. One antenna is used to couple the radio frequency to the cavity. The second one is used to pick up the signal and analyze it with the vector network analyzer. The two other antennas are terminated by a  $50\ \Omega$  load. The vector network analyzer is stabilized with a rubidium clock from Stanford Research, which in turn is stabilized using the pps-signal of the GPS satellite network.



(a) Open cavity: The flange is removed to reveal the striplines (parallel plates), wings and antennae.

(b) Installed cavity with coils and the bottom half of the three layer magnetic shielding.

Figure 8: Microwave cavity.

### 3.8 Analysis Magnets

The analysis magnets have two purposes: State selection of the beam after the cavity, and focussing of the beam onto the detector. In configuration 1 of the hydrogen beam experiment the superconducting sextupole magnet was used. Information regarding the superconducting sextupole can be found in [19]. In the second configuration of the hydrogen beam experiment the SMI magnets have been used. They consist of an array of permanent magnets in a Halbach configuration and are described in detail in chapter 4.

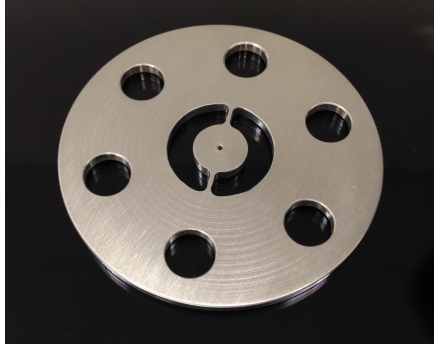
### 3.9 Ring Aperture

Two ring apertures (figure 9) are used to select atoms at a defined radius and to block the central part of the beam. They have got a hole of 1 mm diameter in the center to allow the laser to pass through. The apertures are aligned with respect to the laser by optical means. Both ring apertures have been manufactured at the SMI workshop.

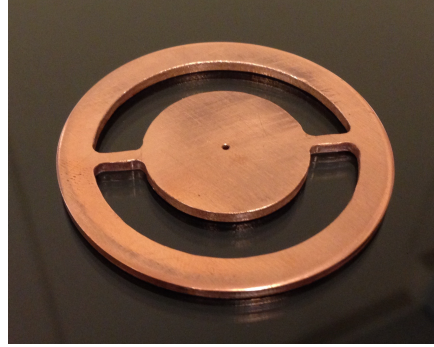
### 3.10 Detector

The beam of hydrogen atoms is detected with a quadrupole mass spectrometer (QMS), which is mounted perpendicular to the beam axis. A hole of 3 mm diameter allows the beam to enter the QMS. The model MKS Microvision2 RGA is used.

Electrons are emitted from a filament, collide with the hydrogen atoms and ionize them. The resulting proton enters the analyzer of the quadrupole mass spectrometer. The selected mass of the QMS is set to 1 atomic mass unit. The proton, therefore, can pass the analyzer and cause a signal at the channeltron while a large fraction of ionization products from residual gas is



(a) Ring aperture 1 with an inner diameter of 12 mm and an outer diameter of 20 mm.



(b) Ring aperture 2 with an inner diameter of 23 mm and an outer diameter of 38 mm.

Figure 9: Ring apertures. The 1 mm hole in the center is used for alignment purposes.

suppressed.

The resulting signals of the channeltron are amplified and converted to a digital signal using NIM modules and counted with a NI PCIe-6361 data acquisition card. The data is transferred to the measurement PC, and the counts are processed by the lock-in amplifier program. Further information on the data acquisition scheme can be found in [26].

### 3.11 Setup Configurations of the Hydrogen Beam Experiment

Several configurations of the hydrogen beam experiment have been used and are discussed in multiple sections of this work. An overview of their characteristics and differences is provided in this section.

The antihydrogen setup is not discussed in detail in this work. For a reference see [19] and references therein.

#### 3.11.1 Configuration 1

This setup consists of: the hydrogen source, the CERN magnets, the chopper, cavity 1, the superconducting sextupole magnet, and the QMS detector.

It was used to characterize the spectroscopy apparatus, consisting of cavity 1 and the superconducting sextupole magnet, for antihydrogen operation [23, 25, 26].

#### 3.11.2 Configuration 2.1 "Permanent Magnets"

This setup (figure 10) consists of: the hydrogen source, the CERN magnets, the chopper, cavity 2, the SMI magnets, and the QMS detector. The setup

is different from configuration 1 in two aspects:

Cavity 1 is replaced by cavity 2, which is identical in construction. However, 4 McKeehan coils instead of 2 Helmholtz coils are used to produce a more homogeneous magnetic field inside the cavity. The coils are arranged such that there is a component of the constant field in direction of the oscillating field as well as perpendicular to the oscillating field, which enables both  $\sigma$ - and  $\pi$ -transitions to occur.

The superconducting sextupole magnet is replaced by several SMI magnets. Five of the SMI magnets are used, they have a similar integrated gradient as the superconducting sextupole magnet at a current of 350 A. The inner diameter of the SMI magnets is 40 mm, much smaller than the inner diameter of the superconducting sextupole magnet. This is not a problem for the hydrogen beam, because it is limited by the opening of the chopper rather than by the inner diameter of the SMI magnets.

Configuration 2.1 was used to measure simultaneously the  $\sigma$ - and  $\pi$ -transition in earth's magnetic field (see chapter 7).

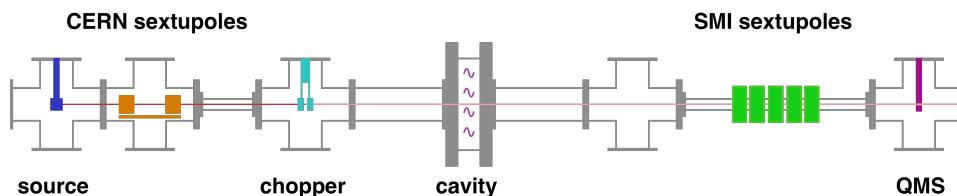


Figure 10: Beam line configuration 2.1: "permanent magnets".

### 3.11.3 Configuration 2.2 "Short Setup"

This setup (figure 11) consists of: the hydrogen source, the CERN magnets, the chopper, the SMI magnets, and the QMS detector. The difference between this setup and configuration 2.1 is the following:

Cavity 2 was removed because some modifications were necessary, which were made at the CERN workshop. Therefore, the beam line was shortened accordingly.

Configuration 2.2 was used for tests of the new SMI magnets and to evaluate the velocity selecting properties of the CERN magnet assembly (see chapter 5).

### 3.11.4 Configuration 2.3 "Ring Aperture"

This setup (figure 12) consists of: the hydrogen source, the chopper, ring aperture 1, three SMI magnets, cavity 2, ring aperture 2, two SMI magnets, and the QMS detector. The difference of this setup from configuration 2.1 is the following:

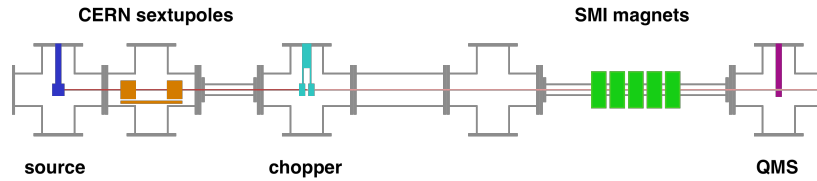


Figure 11: Beam line configuration 2.2: "short setup".

The CERN magnets for velocity selection are replaced by a different method for velocity selection: The divergent beam passes a ring shaped aperture (aperture 1) and is made parallel by three SMI magnets. The parallel beam passes the cavity and a second ring shaped aperture (aperture 2). The second ring aperture selects hydrogen atoms in a very narrow band of velocities, which are defined by the geometry and the strength of the first three SMI magnets. Then the two SMI magnets focus the beam onto the detector. For this setup it is necessary to mount the chopper as close to the source as possible because the beam diameter of the divergent beam is already considerably large at the chopper position. For trajectories of hydrogen atoms in this configuration see section 6.7.

Configuration 2.3 was used to measure simultaneously the  $\sigma$ - and  $\pi$ -transition in earth's magnetic field (see chapter 7).

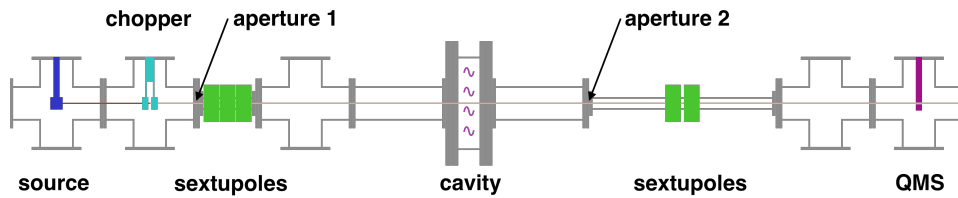


Figure 12: Beam line configuration 2.3: "ring aperture".

## 4 Magnetic Field Measurement of Analysis Sextupole Magnets

For charged particle beams, sextupole magnets are commonly used to correct for chromatic aberrations. However, for beams of neutral particles with magnetic moment, sextupole magnets act as a (velocity dependent) focusing lens. The focusing effect on neutral particles with magnetic moment  $\vec{\mu}$  is described in detail in chapter 6.

The hydrogen beam experiment makes use of several identical permanent sextupole magnets to focus the beam of hydrogen atoms onto the detector. These magnets are built at SMI utilizing a Halbach-like configuration of cuboid permanent magnets. In order to characterize the quality of the sextupole magnetic field of these magnets, maps of the magnetic field of several sextupole magnet assemblies are recorded and analyzed.

### 4.1 Magnetic Field of an Ideal Sextupole

Because of  $\nabla \times \vec{B} = 0$  in the inner area of an ideal sextupole magnet, the magnetic field can be expressed as gradient of a scalar magnetic potential  $\Phi(x, y, z)$ . For an (in  $z$ -direction) infinitely extended sextupole the scalar potential is

$$\Phi(x, y, z) = \frac{g_s}{2} \left( x^2 y - \frac{y^3}{3} \right) \quad (70)$$

where  $g_s$  is a constant that describes the strength of the sextupole field. Using  $\vec{B} = -\vec{\nabla}\Phi$  the components of the sextupole field are calculated as

$$B_x = g_s xy, \quad (71)$$

$$B_y = \frac{g_s}{2} (x^2 - y^2), \quad (72)$$

$$B_z = 0. \quad (73)$$

The absolute value of the sextupole field depends only on the square of the radius and the constant  $g_s$ :

$$|\vec{B}| = \frac{|g_s|}{2} r^2. \quad (74)$$

### 4.2 SMI Sextupole Magnets

A hollow cylinder with magnetization

$$\vec{M}(\rho, \phi, z) = M_r \left( \cos(k\phi) \hat{\rho} + \sin(k\phi) \hat{\phi} \right), \quad k \in \mathbb{Z} \quad (75)$$

is called an ideal Halbach cylinder [40–43]. The magnetization of the ideal Halbach cylinder generates flux only on one side, producing either a strong

magnetic field confined inside the cylinder with zero magnetic field outside, or a strong magnetic field outside the cylinder with zero magnetic field inside. In the above equation  $|k|$  is the number of pole pairs, the sign of  $k$  is positive for magnetic fields inside of the cylinder and negative for magnetic fields outside of the cylinder.

For a dipole, the magnetic field within the cylinder is given by

$$B = B_R \ln \left( \frac{r_o}{r_i} \right) \quad (76)$$

where  $B_R$  is the remanence of the magnetic material,  $r_i$  and  $r_o$  the inner and outer radius, respectively. To achieve large magnetic fields,  $B_r$  and the ratio of outer to inner radius  $\frac{r_o}{r_i}$  need to be large.

Magnets with continuously varying magnetization are not easy to produce, therefore, the ideal Halbach cylinder is usually approximated using segments of uniformly magnetized material. The design of the SMI permanent sextupole magnets [44] uses 12 cuboid magnets with uniform magnetization which are arranged in a circular pattern to get a magnetization close to the ideal Halbach cylinder.

The cuboid magnets are made of blocks of NdFeB material  $15 \text{ mm} \times 15 \text{ mm} \times 50 \text{ mm}$  in size [45] and are magnetized along the short direction. In the sextupole assembly (figure 13) the 12 NdFeB magnets are supported by a 3d-printed holder (green) and mounted onto the beam pipe with the aluminum enclosing. From a large batch of magnets groups of 12 magnets with homogeneous properties are selected for the individual Halbach arrays.

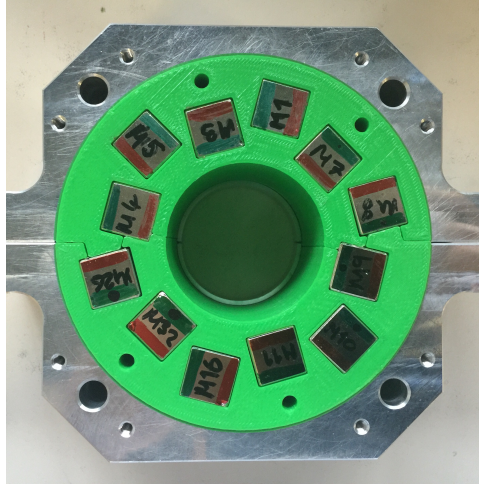


Figure 13: SMI sextupole magnet of configuration A.

The SMI sextupole assembly deviates from the circular Halbach approximation in that sense that every second magnet is shifted inwards. There are two possible configurations to realize this. In configuration A the magnets

with magnetization in radial direction are shifted inwards, while in configuration B the magnets with tangential magnetization are shifted inwards. The layout of these two versions is depicted in figure 14.

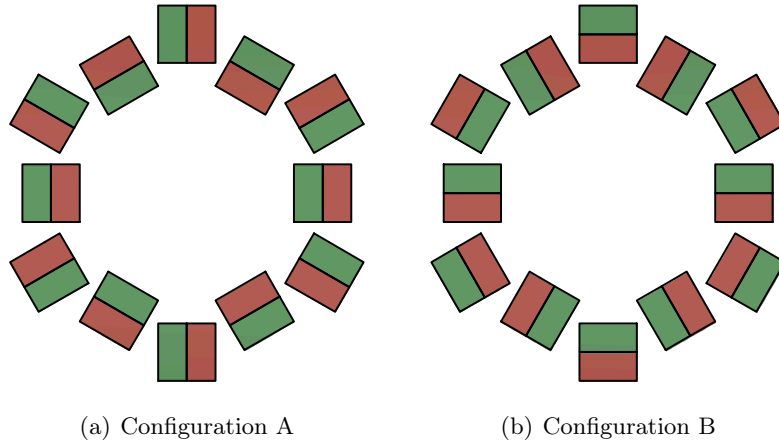


Figure 14: Configuration A and configuration B of magnet assembly.

### 4.3 Measurement Device

To characterize the magnetic field of the sextupole magnet assembly, a device to accurately take measurements of the magnetic field inside the cylindrical hole was built (figure 15).

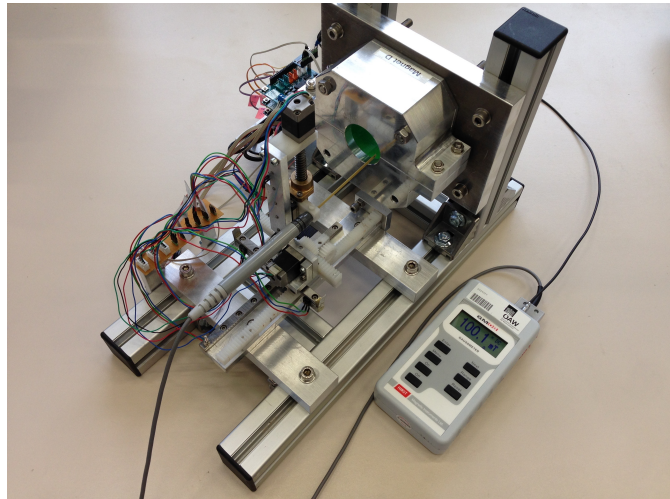


Figure 15: Device to record field maps of SMI sextupole magnets.

A mounting plate to attach the magnet assembly and a 3d positioning system are mounted on a common aluminum frame, manufactured by the

SMI workshop. The mounting plate is designed to allow the magnet assembly to be rotated by  $90^\circ$ ,  $180^\circ$  and  $270^\circ$ . The 3d positioning system is used to scan the cylindrical volume inside the sextupole magnet with a magnetic field sensor.

The hardware for the 3d positioning system was reused from an earlier experiment, but the electronics and the software to control the 3 axes had to be developed. Every single axis is manipulated by a stepper motor [46]. Arduino motor shields [47] are used to drive the stepper motors. An Arduino Leonardo board [48] with an ATmega32u4 microcontroller is used to control the stepper motor drivers.

As a magnetic field sensor a hall probe has been chosen for the very small dimensions of the sensor. The measurements of the magnetic field were recorded using a Hirst GM 08 Gaussmeter with a transverse hall probe [49]. This sensor can only measure the magnetic field in one direction. Therefore, the magnet assembly was rotated on the mounting plate to enable measurements in the perpendicular direction. Measurements of the fields in  $z$ -direction were not taken, because they are comparatively small and less relevant.

#### 4.4 Data Acquisition

The data acquisition scheme is displayed in figure 16. The Hirst GM08 Gaussmeter is able to measure magnetic fields up to 3 T in four measurement ranges (see table 1). The analog output of the Hirst GM 08 Gaussmeter delivers a voltage signal between  $-3\text{ V}$  and  $3\text{ V}$ , which is proportional to the measured magnetic field with a conversion factor which depends on the selected measurement range. This analog signal is digitized using a 16 bit, 4 channel ADS1115 analog to digital converter on an Adafruit board [50].

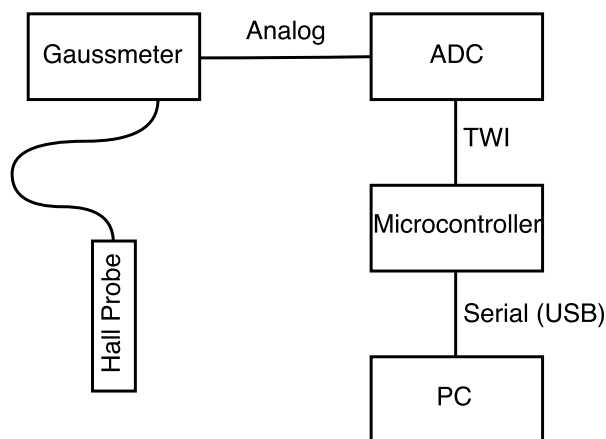


Figure 16: Data acquisition scheme for sextupole field maps.

As the output signal consists of positive and negative voltage values, the differential read out mode between two channels of the ADS1115 is used. The Hirst GM08 Gaussmeter is battery operated.

The digitized values are read out with the microcontroller on the Arduino Leonardo board via two wire interface (TWI). At every coordinate, 100 measurements are taken in succession. The mean  $m$  and standard deviation  $\text{sig}$  are calculated online using the following stable numerical algorithm [51]:

```

m = 0; m2 = 0;
for (int l=0; l<n; ){
value = readadc();
l++;
delta = value - m;
m += delta/l;
m2 += delta * (value - m);
}
m2 = m2/(n-1);
sig = sqrt(m2);

```

It was necessary to implement this algorithm, because the numerical capabilities of the microcontroller are not sufficient to perform the computation according to the usual formulas

$$m = \frac{1}{n} \sum_{i=1}^n x_i, \quad (77)$$

$$\sigma^2 = \frac{1}{n-1} \left( \sum_{i=1}^n x_i^2 - nm^2 \right) \quad (78)$$

where the sum and the sum of the squares are used.

When the measurement at one point is finished, the calculated mean and standard deviation together with the coordinates of the measurement point are transferred to the PC via serial connection (USB) and the positioning stage moves on to the next coordinate. On the PC the values are received and stored in a data file for analysis.

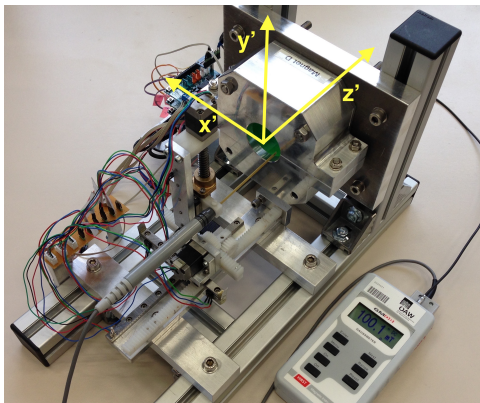
#### 4.5 Field Reconstruction

For all points on a grid of 1.88 mm spacing in  $x$ - and  $y$ -direction and 5.65 mm spacing in  $z$ -direction (see figure 17(b)) that also lie within the cylindrical volume of radius  $r \leq 18$  mm, a measurement of the magnetic field is recorded. The recorded magnetic field measurement of the hall probe is the value of  $B_{x'}(x', y', z')$ , the magnetic field in  $x'$ -direction in the coordinate system  $(x', y', z')$  of the measurement device (see figure 17(a)).

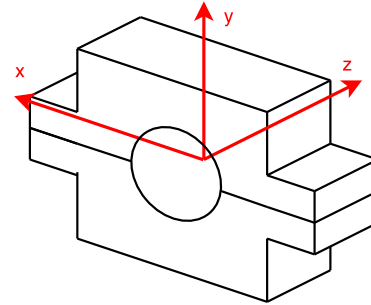
To map the recorded field  $B_{x'}(x', y', z')$  to the coordinate system  $(x, y, z)$  of the magnet, a coordinate transformation has to take place: In the case of  $0^\circ$  rotation the transformation is only a shift in  $z$ -direction.

Specification	Value
Range 1	0.000 - $\pm 3.000$ Tesla
Range 2	000.0 - $\pm 299.9$ milliTesla
Range 3	00.00 - $\pm 29.99$ milliTesla
Range 4	0.000 - $\pm 2.999$ milliTesla
Frequency Range	DC and 15Hz to 10kHz
DC Accuracy	Better than $\pm 1$ % Probe and Gaussmeter (NPL Traceable)
Temperature coefficient	Better than $\pm 0,1$ % of reading / $^{\circ}\text{C}$ including probe
Analogue Output	$\pm 3$ Volts full scale

Table 1: Excerpt of technical specifications of Hirst GM 08 Gaussmeter [49].



(a)  $(x', y', z')$  coordinates



(b)  $(x, y, z)$  coordinates

Figure 17: Coordinate system of measurement device and coordinate system of SMI sextupole magnet.

After recording  $B_{x'}(x', y', z')$  the magnet is rotated by  $90^\circ$  on the holder and  $B_{x'}(x', y', z')$  is measured again. However, now the measurement of  $B_{x'}(x', y', z')$  in the coordinate system of the measurement device corresponds to  $B_y$  in the coordinate system of the magnet. After that, measurements with the magnet rotated by  $180^\circ$  and  $270^\circ$  are recorded as well. The coordinate transformations for all four rotations are summarized in table 2.

angle	$0^\circ$	$90^\circ$	$180^\circ$	$270^\circ$
$x =$	$x'$	$-y'$	$-x'$	$y'$
$y =$	$y'$	$x'$	$-y'$	$-x'$
$z =$	$z' - z_{\text{offset}}$	$z' - z_{\text{offset}}$	$z' - z_{\text{offset}}$	$z' - z_{\text{offset}}$
$B_x =$	$B_{x'}$	0	$-B_{x'}$	0
$B_y =$	0	$B_{x'}$	0	$-B_{x'}$

Table 2: Coordinate transformations for the four different angles of rotation of the magnet. The offset  $z_{\text{offset}} = 42.5$  mm.

After these four field maps are recorded, two values for each  $B_x$  or  $B_y$  are available (one value for  $0^\circ$  rotation denoted  $B_{x,0}$  and one for  $180^\circ$  rotation denoted  $B_{x,180}$ ). For the rest of the analysis the mean of both values is taken. This leads to the cancellation of errors from a background field, a sensor offset, and a position offset, as can be seen as follows:

The mean

$$B_x = \frac{1}{2}(B_{x,0} + B_{x,180}) \quad (79)$$

actually corresponds to

$$B_x = \frac{1}{2}(B_{x',0} - B_{x',180}) \quad (80)$$

where the second index refers to the rotation in degrees.

If a sensor reading is estimated as:

$$B_{x',0} = B_t + B_{\text{bg}} + B_{\text{so}} \quad (81)$$

$$B_{x',180} = -B_t + B_{\text{bg}} + B_{\text{so}} \quad (82)$$

where  $B_t$  is the true value of the magnetic field produced by the permanent magnets,  $B_{\text{bg}}$  is the magnitude of a time and coordinate independent background field (e.g. earth's magnetic field), and  $B_{\text{so}}$  is the magnitude of a constant sensor offset, this leads to the cancellation of  $B_{\text{bg}}$  and  $B_{\text{so}}$ :

$$B_x = \frac{1}{2}(B_{x',0} - B_{x',180}) \quad (83)$$

$$B_x = \frac{1}{2}(B_t + B_{\text{bg}} + B_{\text{so}} \quad (84)$$

$$-(-B_t + B_{\text{bg}} + B_{\text{so}})) \quad (85)$$

$$B_x = \frac{1}{2}(B_t + B_t) \quad (86)$$

Therefore, this measurement method cancels automatically a time and coordinate independent background field and a constant sensor offset at the same time.

The same argument holds for  $B_y$  as well.

Cancellation of positioning errors: The hall probe is centered to the axis of the magnet at the beginning of the measurement, yet a small offset in position  $\Delta x'$  or  $\Delta y'$  cannot be excluded. If one measurement is taken at the coordinates  $(x, y, z) = (x' + \Delta x', y', z')$ , the rotated measurement is taken at  $(x, y, z) = (-x' + \Delta x', -y', z')$ . Taking the average, this becomes

$$B(x, y, z) = \frac{1}{2}(B'_0(x', y', z') - B'_{180}(-x', -y', z')) \quad (87)$$

$$B(x, y, z) = \frac{1}{2}(B_0(x - \Delta x', y, z) + B_{180}(x + \Delta x', y, z)) \quad (88)$$

which linearly interpolates  $B(x, y, z)$ .

The same argument holds for  $\Delta y'$  and the  $y$ -coordinate as well.

#### 4.6 Analysis Method

The field maps obtained with the reconstruction method described above are used to determine the quality of the SMI permanent sextupoles magnetic field.

As a first step, the equation for the sextupole field

$$B(r) = \frac{g_s}{2} r^2 \quad (89)$$

is fitted to the measurement points for every  $z$ -plane (see figure 18).

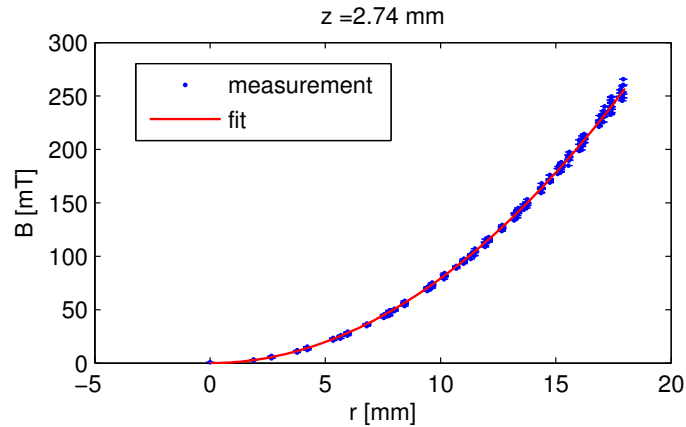


Figure 18: Measured values of the magnetic field of magnet C at  $z = 2.74$  mm and fit of  $B(r) = \frac{g_s}{2} r^2$ .

This results in a value of the sextupole strength  $g_s$  in dependence of the  $z$ -coordinate. It is a measure of the strength of the sextupole field as a

function of the  $z$ -coordinate. As an example the resulting  $z$ -dependence for magnet C is shown in figure 19.

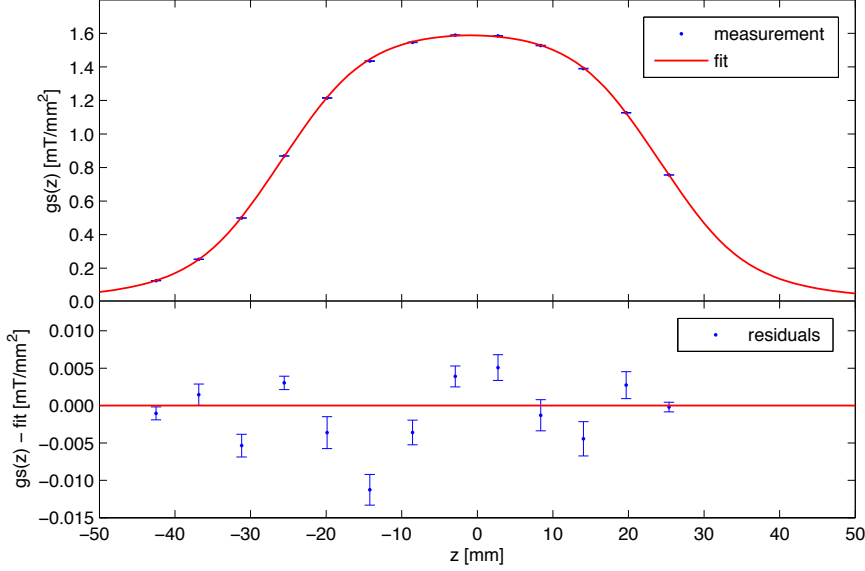


Figure 19: Sextupole strength  $g_s(z)$  of magnet C, determined by fitting all measurements for a given  $z$ -plane, and fit of  $f_4(z)$  (upper graph). Residuals of fit (lower graph).

In the second step, an analytic equation is fitted to the determined values of  $g_s(z)$  in order to get an analytic function of the  $z$ -dependence of the sextupole strength. This function will be used in the trajectory simulations described in chapter 6.

In a third step, the sextupole strength  $g_s(z)$  is integrated along the  $z$ -axis to get a measure of the total strength of the sextupole field

$$G_s = \int_{-\infty}^{+\infty} g_s(z) dz \quad (90)$$

of a magnet and to be able to compare different magnets.

The following functions are evaluated as model for the sextupole strength  $g_s(z)$ :

$$f_1(z) = a \exp\left(-\left(\frac{z-m}{s}\right)^2\right) \left((z-m)^2 + b\right) \quad (91)$$

$$f_2(z) = \frac{a}{2} \left( \frac{z-m+L/2}{\sqrt{R^2+(z-m+L/2)^2}} - \frac{z-m-L/2}{\sqrt{R^2+(z-m-L/2)^2}} \right) \quad (92)$$

$$f_3(z) = \frac{a}{2} (\tanh(b(z-m+L/2)) + \tanh(b(-z+m+L/2))) \quad (93)$$

$$f_4(z) = \frac{a}{2} \left( \frac{z - m + L/2}{(R^c + |z - m + L/2|^c)^{1/c}} - \frac{z - m - L/2}{(R^c + |z - m - L/2|^c)^{1/c}} \right) \quad (94)$$

$$f_5(z) = \frac{a}{\pi} (\arctan(b(z - m + L/2)) + \arctan(b(-z + m + L/2))) \quad (95)$$

where  $m$  is the center of the magnet,  $L$  the length of the magnet,  $a$  describes the magnitude, and  $b$ ,  $c$  and  $R$  are parameters that describe the shape.

Except for  $f_1(z)$  all of these functions are superpositions of functions that go smoothly from 0 to 1 and are symmetrical with respect to a point where they are at half maximum. From theoretical considerations [42] follows that this point should be at the end of the magnet where  $z = \pm L/2$ .

These functions are fitted to measurements of 9 magnets and the root mean squared error<sup>10</sup> (RMSE) of the fit is determined. For every function the mean and standard deviation of the RMSE of these 9 measurements is displayed in table 3. As can be seen from table 3 the function  $f_4(z)$  best describes the measurements.

function	mean of RMSE	standard deviation of RMSE
$f_1(z)$	9.25	1.26
$f_2(z)$	9.63	1.49
$f_3(z)$	5.80	0.78
$f_4(z)$	2.90	0.80
$f_5(z)$	24.6	3.02

Table 3: Root mean squared error (RMSE) of fitting functions.

## 4.7 Comparison of Magnet Configurations

One set of the same 12 NeFeB magnets were used to build first a magnet of configuration A and then of configuration B in order to compare the field of both configurations.

The results are shown in figure 20. The maximum of the sextupole field for configuration A is 5% larger than for configuration B. The full width at half maximum is almost the same for both configurations and is equal to the physical length of the magnets, which is 50 mm. In comparison with configuration B, for configuration A the magnetic field is larger inside the magnet ( $|z| < L/2$ ), than outside of the magnet ( $|z| > L/2$ ).

In table 4 the maximum of the field strength  $g_{s,\max}$ , the integrated gradient and the fitting parameters are summarized for both configurations.

Another advantage of configuration A is the attractive force between the individual magnets. This avoids instabilities during assembly and makes it also preferable from a safety point of view over configuration B, where the

<sup>10</sup>see page 41

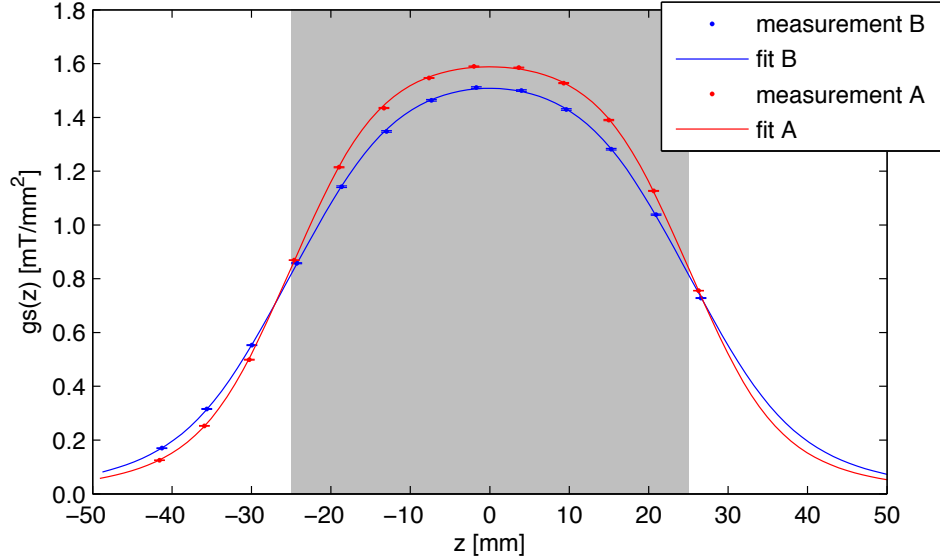


Figure 20: Comparison of  $g_s(z)$  for configuration A (red) and configuration B (blue). Magnet C was used for this comparison. The grey area indicates the physical length of the magnets.

parameter	configuration A	configuration B	unit
$g_{s,\max}$	1.590	1.511	$\text{mT mm}^{-2}$
$G_s$	85.15	83.25	$\text{T m}^{-1}$
$L$	$50.04 \pm 0.11$	$49.99 \pm 0.15$	mm
$R$	$12.68 \pm 0.16$	$15.19 \pm 0.14$	mm
$a$	$1.7017 \pm 0.0077$	$1.6654 \pm 0.0072$	$\text{mT mm}^{-2}$
$c$	$2.473 \pm 0.068$	$2.525 \pm 0.051$	-
$m$	$-0.918 \pm 0.028$	$-1.231 \pm 0.033$	mm

Table 4: Comparison of parameters for configuration A and configuration B. Magnet C was used for this comparison.

magnets strongly repel each other. Because the half shells are held together by the magnetic force, they can be installed at the beam pipe without any screws.

## 4.8 Results

All 9 SMI permanent magnet assemblies have been analyzed using the method described above. The resulting measurements are shown in figure 21 and the results of the fits to the measured values are summarized in table 5.

As can be seen in figure 21, the variation between the individual magnets is very small. There is however one group of magnets (D, E, F and G) for which the amplitude  $a$  is higher by 2%. As expected, for all magnets the length  $L$  at half maximum corresponds to the physical length of the magnets within the error. It is interesting to note that the exponent  $c$  in equation 94 is  $\approx \frac{5}{2}$  for all magnets.

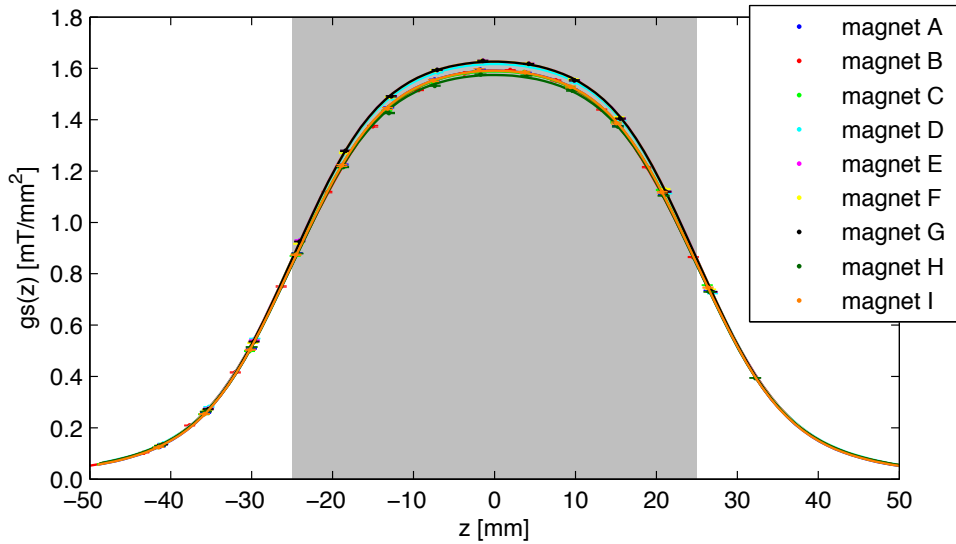


Figure 21: Sextupole strength  $g_s(z)$  for all 9 SMI sextupole magnets. The physical length of the magnets is indicated in grey.

For his summer student report M. Huzan [52] carried out further analysis on the SMI sextupole magnets: The approach is to fit

$$B(x, y) = \frac{g_s}{2} \left( \left( \frac{x - x_0}{a} \right)^2 + \left( \frac{y - y_0}{b} \right)^2 \right) \quad (96)$$

to every  $x$ - $y$ -plane for an individual magnet and to determine  $g_s$  as well as the parameters  $a$ ,  $b$ ,  $x_0$  and  $y_0$  as a function of the  $z$ -coordinate. The parameters  $a$  and  $b$  describe the ellipticity, and the parameters  $x_0$  and  $y_0$  an offset in  $x$ - and  $y$ -direction, respectively.

The results show no ellipticity within the error and no offset in neither  $x$ - nor  $y$ -direction for all 9 SMI magnets.

magnet	$L$ [mm]	$R$ [mm]	$a$ [mT mm <sup>-2</sup> ]	$c$ [1]	$m$ [mm]
A	$49.87 \pm 0.13$	$12.72 \pm 0.17$	$1.7028 \pm 0.0087$	$2.505 \pm 0.076$	$-1.167 \pm 0.031$
B	$49.89 \pm 0.18$	$13.13 \pm 0.22$	$1.7034 \pm 0.0077$	$2.567 \pm 0.077$	$+0.816 \pm 0.060$
C	$50.04 \pm 0.11$	$12.68 \pm 0.16$	$1.7017 \pm 0.0077$	$2.473 \pm 0.068$	$-0.918 \pm 0.028$
D	$50.04 \pm 0.12$	$12.48 \pm 0.14$	$1.7382 \pm 0.0078$	$2.395 \pm 0.061$	$-1.576 \pm 0.033$
E	$49.99 \pm 0.11$	$12.42 \pm 0.14$	$1.7439 \pm 0.0079$	$2.420 \pm 0.063$	$-1.519 \pm 0.029$
F	$49.92 \pm 0.10$	$12.44 \pm 0.12$	$1.7462 \pm 0.0060$	$2.407 \pm 0.047$	$-1.343 \pm 0.026$
G	$49.92 \pm 0.11$	$12.42 \pm 0.13$	$1.7442 \pm 0.0077$	$2.419 \pm 0.061$	$-1.475 \pm 0.030$
H	$49.96 \pm 0.14$	$12.61 \pm 0.16$	$1.6937 \pm 0.0089$	$2.410 \pm 0.069$	$-1.194 \pm 0.032$
I	$49.93 \pm 0.09$	$12.65 \pm 0.11$	$1.7026 \pm 0.0047$	$2.488 \pm 0.036$	$-1.018 \pm 0.025$

Table 5: Fit parameters: results of fitting  $f_4(z)$  to the measurements of  $g_s(z)$  of all 9 SMI magnets.



## 5 Velocity Selection of Polarizing Sextupoles

The hydrogen beam experiment features a permanent sextupole magnet doublet (the CERN magnets) whose purpose is to polarize the beam and to select a narrow band of velocities from the Maxwell-Boltzmann distributed velocities of the hydrogen atoms emitted by the source. In this chapter measurements of the velocity selecting properties of the CERN permanent sextupole magnets are presented.

### 5.1 Setup

This measurement uses the configuration 2.2 "short setup" of the hydrogen beam experiment (see section 3.11.3). The beam of atomic hydrogen from the source is collimated by a 2 mm diameter skimmer. The skimmer is mounted between the source and the CERN magnet doublet with a distance of  $\approx 170$  mm between the skimmer and the CERN magnet doublet. Hydrogen atoms of certain velocities are selected by passing through both magnets and the aperture in between, as described in section 3.5.

The distance between both magnets of the CERN magnet doublet is varied by a rack and pinion gear and a manual rotation feedthrough, which can be locked to a set of mounting holes for reproducibility of each position. A mounting hole  $mh$  corresponds to a distance  $d$  between both magnets of

$$d = 16 \text{ mm} + mh \times 1.875 \text{ mm}. \quad (97)$$

The tuning fork chopper is mounted downstream of the CERN magnet doublet with a distance of 2.2 m between the chopper and the QMS detector. The beam is chopped with a frequency of  $\approx 178.5$  Hz. Five SMI sextupole magnets are used to focus the beam onto the QMS detector.

### 5.2 Method

The setup is aligned by optical means with the help of the laser beam. A beam of hydrogen atoms is introduced into the setup. The chopper is activated and its amplitude set close to its maximum amplitude. The alignment of the QMS detector is adjusted in the plane perpendicular to the beam such that the rate at the detector is at a maximum.

Then the distance between the two CERN sextupole magnets is varied in steps of 5 mounting holes. For every step several sets of histograms of count rate versus chopper phase are recorded by the software lock-in amplifier. The recording time for one histogram was set to 60 s. The number of histograms recorded for every step is shown in table 6.

At the end of the measurement campaign the QMS detector is adjusted in the plane perpendicular to the beam such that the laser signal is a maximum. Then the chopper amplitude is varied within  $\pm 10\%$  of the original amplitude and histograms of the laser signal are recorded.

# of measurement	mounting hole	# of histograms
1	40	50
2	45	50
3	50	100
4	35	50
5	30	50
6	15	5
7	20	5
8	25	5
9	31	5
10	10	5
11	5	5
12	0	5
13	5	10
14	0	10
15	10	10
16	20	10
17	25	10
18	15	10
19	35	30
20	30	30
21	40	30
22	45	60
23	50	60

Table 6: List of velocity selection measurements. The measurement number together with the mounting hole setting and the number of recorded histograms are listed. The recording time of one histogram is 60 s.

### 5.3 Analysis

The beam velocity  $v$  is calculated from the time of flight  $t$  of the hydrogen atoms traversing the distance  $L$  between the chopper and the QMS detector. Because the time of flight of the laser signal is negligible, it corresponds directly to the chopper opening. Therefore, comparison of the phase of the laser  $\phi_L$  signal and the phase of the beam signal  $\phi$  with respect to the chopper reference signal with frequency  $f_{ch}$  yields the time of flight. The velocity becomes

$$v = \frac{L}{t} = \frac{L 2\pi f_{ch}}{\phi - \phi_L} \quad (98)$$

where  $\phi$  and  $\phi_L$  are in units of rad.

#### 5.3.1 Laser Phase

The phase of the reference signal of the chopper does not correspond directly to the phase of the opening of the chopper. Therefore, the phase of the opening is determined by the signal of the chopped laser beam on the photo diode. The shift relative to the chopper reference signal is referred to as laser phase.

The laser phase is determined from histograms of the photo diode signal (figure 22). The laser signal is truncated, because the laser beam is smaller in diameter than the chopper opening. Therefore, the photo diode signal is fitted with a truncated positive half-wave of a sine, and the phase is extracted from the fit.

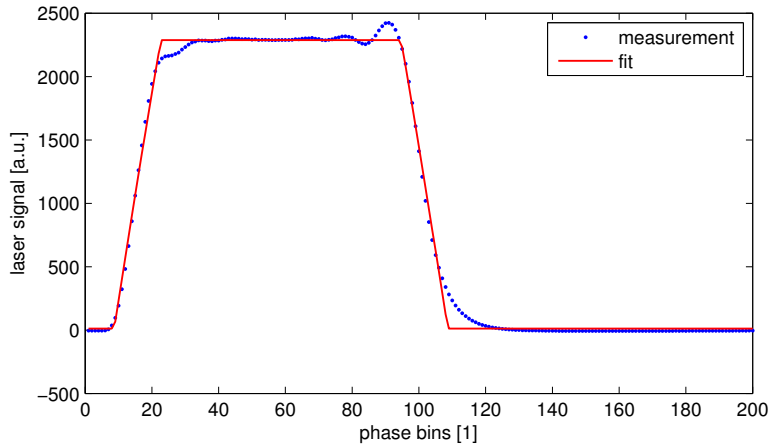


Figure 22: Lock-in amplifier histogram of the laser signal. The fit with a truncated positive half-wave of a sine yields the laser phase.

The laser signal, however, is not always available when the QMS detector is adjusted to the maximum of the hydrogen beam signal. Therefore, a linear

relationship between the laser phase and the chopper frequency is used to reconstruct the laser phase when the laser signal is not available.

To determine the relationship between laser phase and chopper frequency, histograms of the laser signal for several different chopper amplitudes are fitted with the method described above. The values for the laser phase extracted from the fits are shown in figure 23 as a function of the chopper frequency.

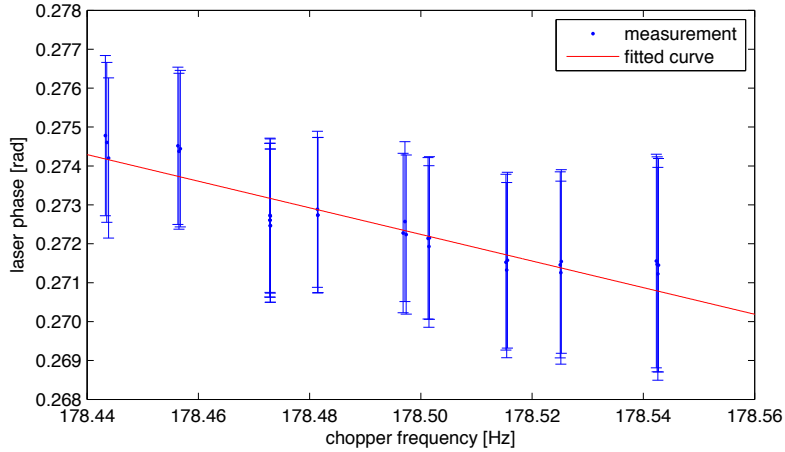


Figure 23: Measurements of laser phase as a function of copper frequency.

A model for prediction of the laser phase

$$\phi_L[\text{rad}] = a \times (f_{ch}[\text{Hz}] - 178.5) + b \quad (99)$$

is fitted to the data. The results for the coefficients  $a$  and  $b$  are:

$$a = -0.0342 \pm 0.0030 \quad (100)$$

$$b = +0.2722 \pm 0.0001 \quad (101)$$

An estimated value of the laser phase using this equation is used when the laser signal is not available.

### 5.3.2 Beam Phase

The lock-in amplifier returns histograms of count rate versus phase of the reference signal (figure 24). The count rate shows two components: a constant background, and the signal of the beam, which is modulated with the chopper frequency. The beam phase is determined from these histograms by fitting a suitable function, where the beam phase is a fit parameter. Several fit functions are evaluated:

- a positive half-wave of a sine.

- a truncated positive half-wave of a sine (as used for the laser signal).
- a truncated positive half-wave of a sine convoluted with a gaussian.

All three fit functions allow for a determination of the beam phase, from which the mean velocity of the hydrogen beam can be calculated. However, only the last one also allows for the determination of the width of the velocity distribution. The width of the velocity distribution is determined by the fit parameter sigma of the gaussian.

As an example the histogram of beam counts for measurement 1 (table 6), fitted with a positive half-wave of a sine is shown in figure 24. The same histogram, fitted with a truncated positive half-wave of a sine is shown in figure 25. And the fit of the truncated positive half-wave of a sine convoluted with a gaussian is shown in figure 26.

The following goodness-of-fit parameters are calculated to evaluate the three fit functions:

- SSE: sum of squares due to error

$$\text{SSE} = \sum_{i=1}^n w_i (x_i - \hat{x}_i)^2 \quad (102)$$

where  $w_i = 1/\sigma_i^2 = 1/x_i$  the weight,  $x_i$  the measurement and  $\hat{x}_i$  the prediction.

- DOF: residual degrees of freedom
- RMSE: root mean squared error

$$\text{RMSE} = \sqrt{\frac{\text{SSE}}{\text{DOF}}} \quad (103)$$

The RMSE is also known as the square root of the reduced  $\chi^2$ .

Table 7 shows the goodness-of-fit parameters for the three fit functions. Measurement # 1 was used for this evaluation. From the values of the RMSE can be deduced that the truncated sine is a much better fit function than the sine. Best is the convolution of the truncated sine with a gaussian.

fit function	SSE	DOF	RMSE
sine	556.6	197	1.68
trunc	272.7	196	1.18
conv	233.2	195	1.09

Table 7: Goodness-of-fit parameters for the three different fit functions. Sine: Positive half-wave of sine. Trunc: Truncated positive half-wave of sine. Conv: Convolution of truncated positive half-wave of sine with gaussian.

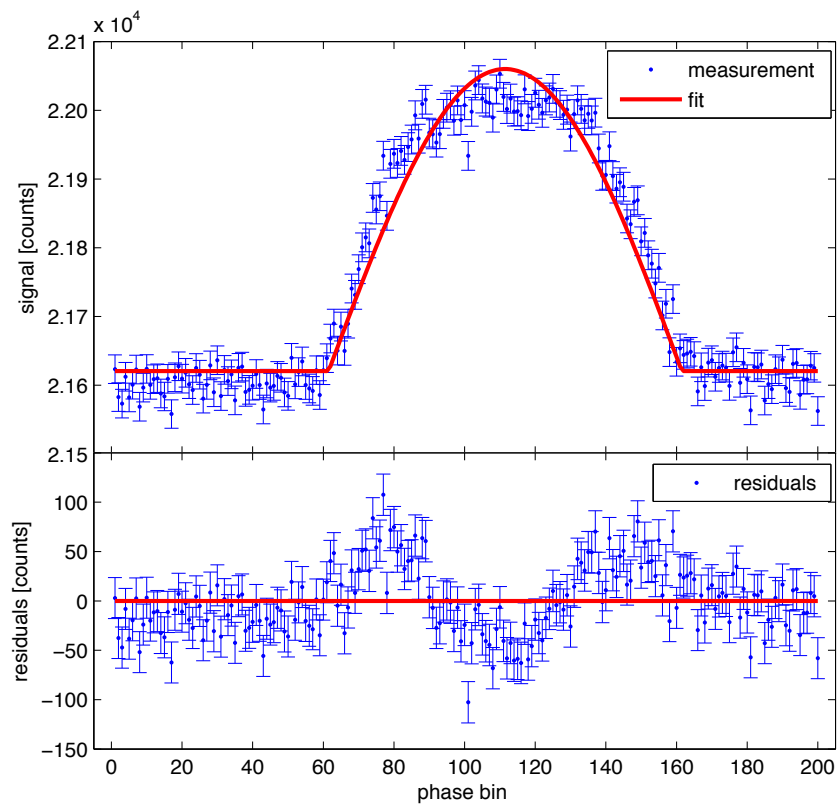


Figure 24: Histogram of count rate versus phase of reference signal (measurement # 1). Top: Count rate and fit with positive half-wave of a sine. Bottom: Residuals of fit.

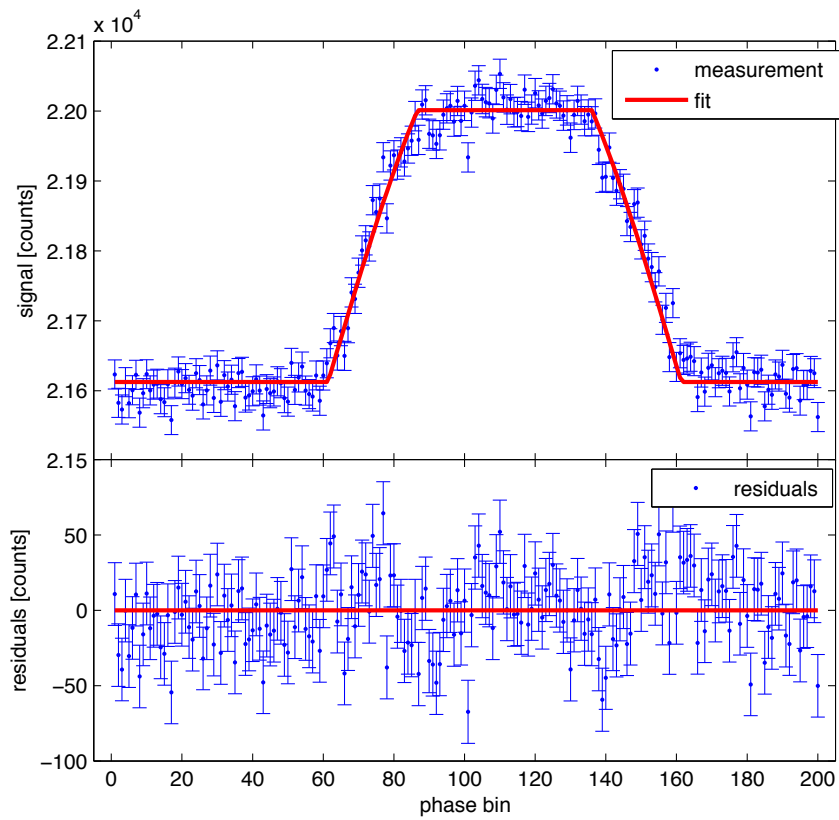


Figure 25: Histogram of count rate versus phase of reference signal (measurement # 1). Top: Count rate and fit with truncated positive half-wave of a sine. Bottom: Residuals of fit.

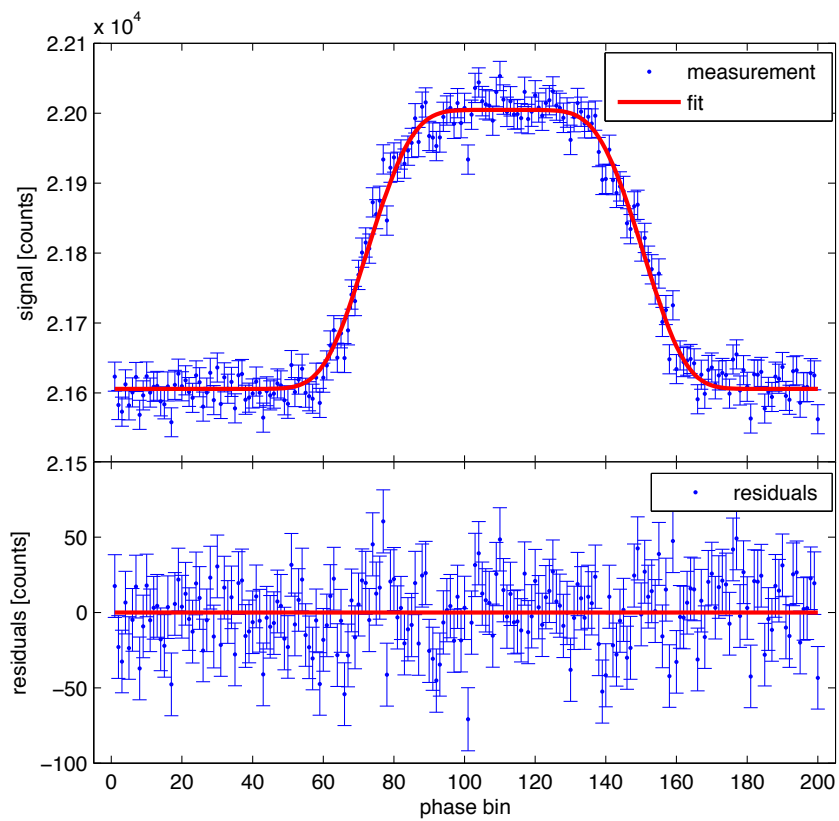


Figure 26: Histogram of count rate versus phase of reference signal (measurement # 1). Top: Count rate and fit with truncated positive half-wave of a sine convoluted with a gaussian. Bottom: Residuals of fit.

## 5.4 Result

For 23 measurements (see table 6) the beam phase  $\phi$  and the laser phase  $\phi_L$  are determined according to the methods described above. The chopper frequency is determined by the lock-in amplifier software and read from the log files of the measurement. The flight path is determined by the setup configuration and 2.2 m long.

The velocities calculated according to equation 98 are plotted against the distance between the CERN sextupole magnets in figure 27. The beam velocity varies linearly between approximately  $1200 \text{ ms}^{-1}$  for the smallest distance and approximately  $1600 \text{ ms}^{-1}$  for the largest distance. The results are independent of the fit function used.

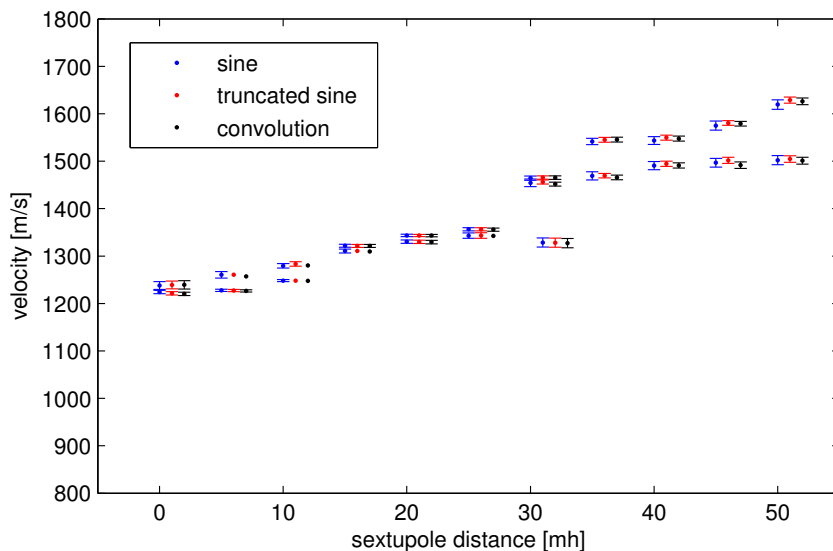


Figure 27: Beam velocity versus distance between the CERN magnet doublet. The colors indicate the fit function used. Red points (truncated sine) have been shifted to the right by one unit for better visibility. Black points (convolution) have been shifted to the right by two units.

Typical relative errors of the physical quantities that enter equation 98 are listed in table 8. The largest contributions come from the laser phase and the beam phase. The relative error of the calculated velocity values is approximately 0.02.

Systematic errors that have not been taken into account and may influence the estimate of velocity:

- Ionic delay: A delay in the signal of the QMS detector due to the time of flight of the ions from the ionization region to the channeltron. A delay would increase the velocity estimates.

quantity	symbol	relative error
length	$L$	0.005
chopper frequency	$f_{ch}$	0.0001
beam phase	$\phi$	0.01
laser phase	$\phi_L$	0.01
velocity	$v$	0.02

Table 8: Typical relative errors of quantities entering the velocity measurements and typical estimated error of calculated velocity values.

- Diode delay: A delay in the signal of the photo diode. A delay would decrease the velocity estimates.
- Beam components with different velocity distributions: The approximation of a gaussian velocity distribution would not be valid any more. A deconvolution analysis of the count rate signal may be attempted.

The results in section 7.5 show that the velocities, determined using this method, are potentially overestimated by 2-13%.

## 6 Trajectory Simulations

To obtain a quantitative understanding of the optical characteristics of the beam line and the transport of atoms through our setup, a simplified model of the hydrogen beam is created. It is presented in this chapter.

### 6.1 Force on Hydrogen Atoms

The force acting on a particle in a static inhomogeneous magnetic field  $\vec{B}$  and a static inhomogeneous electric field  $\vec{E}$  is

$$\vec{F} = q(\vec{E} + \vec{v} \times \vec{B}) - \vec{\nabla}(E) \quad (104)$$

where  $q$  is the charge of the particle,  $\vec{v}$  its velocity, and  $E$  the energy of the particle in the electric and magnetic field. The first term is the Lorentz force. The second term results from the potential energy of the electric and magnetic moment of the particle in the electric and magnetic field, respectively.

Classically the energy may be

$$E = -\vec{d} \cdot \vec{E} - \vec{\mu} \cdot \vec{B} \quad (105)$$

where  $\vec{d}$  is the electric dipole moment and  $\vec{\mu}$  the magnetic moment.

However, for a quantum mechanical system such as the hydrogen atom, the energy is the solution of the eigenvalue problem<sup>11</sup>  $H|\Phi\rangle = E_n|\Phi\rangle$  (equation 25), therefore

$$E = E_n. \quad (110)$$

The force acting on the neutral hydrogen atom in an inhomogeneous magnetic field is

$$\vec{F} = -\vec{\nabla}(E_n). \quad (111)$$

Inserting the eigen energy for the states  $|2\rangle$  and  $|4\rangle$  into equation 111, the force becomes

$$\vec{F} = \mp \mu' \frac{B/B_C}{\sqrt{1 + (B/B_C)^2}} \vec{\nabla} B \quad (112)$$

where  $B = |\vec{B}|$ , the upper sign is for state  $|2\rangle$  and the lower one for state  $|4\rangle$ .

<sup>11</sup>For the hydrogen atom in its ground state the solutions of the eigenvalue problem are the eigen energies (see section 2.1):

$$E_1 = + \frac{h\nu_0}{4} + \mu B \quad (106)$$

$$E_2 = - \frac{h\nu_0}{4} + \mu' B_C \sqrt{1 + (B/B_C)^2} \quad (107)$$

$$E_3 = + \frac{h\nu_0}{4} - \mu B \quad (108)$$

$$E_4 = - \frac{h\nu_0}{4} - \mu' B_C \sqrt{1 + (B/B_C)^2} \quad (109)$$

where  $B$  denotes the absolute value of the magnetic field.

Note that the force does depend on both the absolute value of the magnetic field and the gradient of the absolute value of the magnetic field.

For the states  $|1\rangle$  and  $|3\rangle$  the resulting force is

$$\vec{F} = \mp\mu\vec{\nabla}B \quad (113)$$

where the upper sign is for state  $|1\rangle$  and the lower sign for state  $|3\rangle$ . In this case the force depends only on the gradient of the absolute value of the magnetic field.

## 6.2 Equations of Motion

Equations of motion for the hydrogen atom in state  $|1\rangle$ ,  $|2\rangle$ ,  $|3\rangle$ , or  $|4\rangle$  in the magnetic sextupole field of the beam line are derived. To treat the problem, cylindrical coordinates  $(r, \varphi, z)$  are chosen. The  $z$ -axis is coaxial to the beam and is positive in flight direction.

The magnetic field gradient of the sextupole field

$$\vec{\nabla}B = \vec{\nabla}\frac{g_s}{2}r^2 = g_s r \vec{e}_r \quad (114)$$

points in radial direction ( $\vec{e}_r$  is the unit vector in radial direction). Its strength  $g_s(z)$  is a function of  $z$ .

Effects of the gradient at the end of the magnets, where the gradient points in  $z$ -direction, are neglected.

The equation of motion for states  $|1\rangle$  and  $|3\rangle$  becomes

$$m\ddot{r}\vec{e}_r = \mp\mu\vec{\nabla}B = \mp\mu g_s r \vec{e}_r \quad (115)$$

$$m\ddot{z}\vec{e}_z = 0 \quad (116)$$

and for states  $|2\rangle$  and  $|4\rangle$

$$m\ddot{r}\vec{e}_r = \mp\mu' \frac{B/B_C}{\sqrt{1 + (B/B_C)^2}} \vec{\nabla}B \quad (117)$$

$$= \mp\mu' \frac{g_s r^2 / 2B_C}{\sqrt{1 + (g_s r^2 / 2B_C)^2}} g_s r \vec{e}_r \quad (118)$$

$$m\ddot{z}\vec{e}_z = 0 \quad (119)$$

In the field of the magnetic sextupole, the acceleration in  $z$ -direction is zero, therefore the velocity along the beam axis is constant.

The acceleration in radial direction depends on the radius. For a hydrogen atom in a sextupole field of strength  $g_s = 1600 \text{ T m}^{-2}$  (the typical strength of the SMI magnets) the relative acceleration  $\ddot{r}/r$  for state  $|1\rangle$  and  $|2\rangle$  is shown in figure 28. The acceleration divided by the radius is constant for state  $|1\rangle$ . For state  $|2\rangle$  it depends strongly on the radius, because the

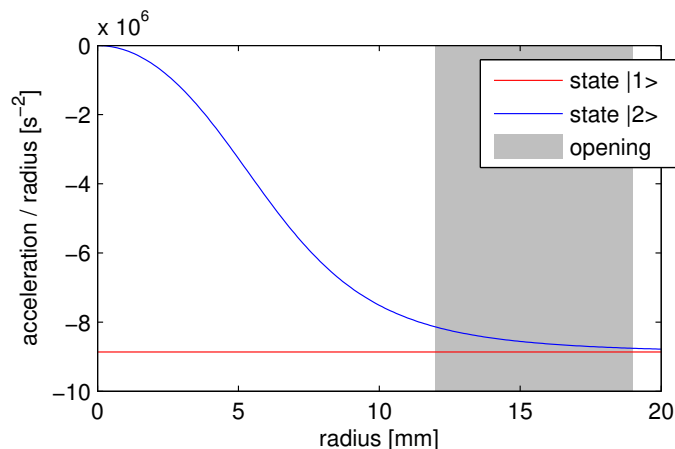


Figure 28: Relative acceleration  $\ddot{r}/r$  in radial direction for hydrogen atoms in state  $|1\rangle$  or  $|2\rangle$  within a sextupole field of  $g_s = 1600 \text{ T m}^{-2}$  (the typical field strength of the SMI magnets). Indicated in grey is the opening of the ring aperture.

magnetic moment depends on the magnetic field, which – in the sextupole magnet – depends on the radius.

For states  $|3\rangle$  and  $|4\rangle$  with positive sign, the motion in radial direction is directed outwards, such that these states are defocused. For the special case of state  $|3\rangle$  and constant  $g_s$ , the solution of the radial equation is described by hyperbolic functions.

For states  $|1\rangle$  and  $|2\rangle$  with negative sign, the motion in radial direction is an oscillation around the beam axis. For a constant  $g_s$ , the motion of state  $|1\rangle$  is a harmonic oscillation. For state  $|2\rangle$  the motion is still an oscillation, but because of the magnetic field dependence of the magnetic moment, it is an anharmonic oscillation.

The behavior described above is shown in figure 29. Trajectories of all four states are plotted for a hypothetical sextupole field of 400 mm length and  $g_s = 114\,000 \text{ T m}^{-2}$  (the typical strength of the CERN magnets). A feature of the harmonic oscillation of state  $|1\rangle$  is, that the oscillation frequency is independent of the radius. Therefore, a beam of state  $|1\rangle$  emerging from a point-like source will get refocussed onto a single point independent of the initial angle, whereas the focal point of state  $|2\rangle$  strongly depends on the initial angle. For large initial angles both trajectories are close, because the deflection happens mostly in the area where the field (and the radius) is large and the acceleration is similar for both states.

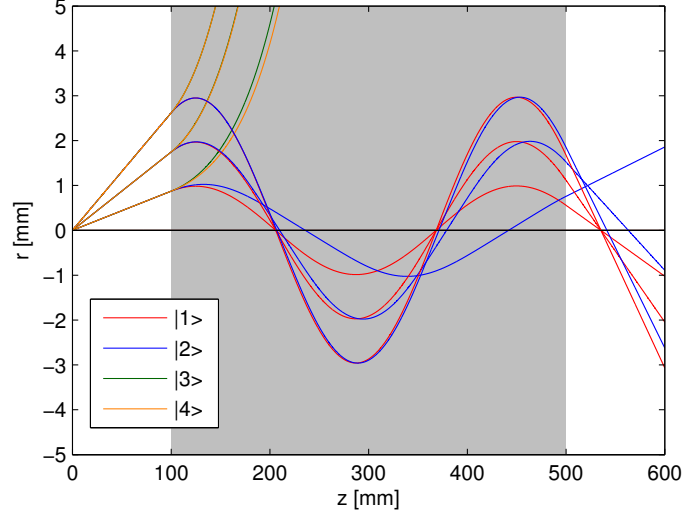


Figure 29: Trajectories of the four ground states of atomic hydrogen in a magnetic sextupole field of strength  $g_s = 114\,000 \text{ T m}^{-2}$  extended from 100 mm to 500 mm (indicated in grey). The initial velocity is  $v_i = 1300 \text{ m s}^{-1}$  and the angles  $\alpha$  between  $v_i$  and the  $z$ -axis are  $\alpha = 0.5^\circ, 1^\circ, \text{ and } 1.5^\circ$ . States  $|1\rangle$  and  $|2\rangle$  oscillate around the beam axis, while states  $|3\rangle$  and  $|4\rangle$  are deflected radially outwards.

### 6.3 Numerical Algorithm

The above equations of motion for hydrogen atoms in their particular state are solved numerically using the Euler method.

The problem is to simultaneously solve

$$\ddot{r}(t) = \frac{\mu_H g_s}{m} r(t) \quad (120)$$

$$\ddot{z}(t) = 0 \quad (121)$$

where  $\mu_H = \mu_H(r, g_s)$  stands for  $\mp\mu$  or  $\mp\mu' \frac{g_s r^2 / 2B_C}{\sqrt{1 + (g_s r^2 / 2B_C)^2}}$ .

Because the solution for the second equation is

$$z(t) = vt \quad (122)$$

where  $v$  is the initial velocity in  $z$ -direction, the radial coordinate  $r$  can be expressed as a function of  $z$

$$r''(z) = \frac{\mu_H g_s}{mv^2} r(z) \quad (123)$$

The second order differential equation can be transformed to two first

order equations

$$r' = k \quad (124)$$

$$k' = \frac{\mu_H g_s}{mv^2} r \quad (125)$$

by introducing  $r' = k$ .

The Euler method for the radial coordinate is then

$$r_{n+1} = r_n + l k_n \quad (126)$$

$$k_{n+1} = k_n + l \frac{\mu_H (r_n, g_s(z)) g_s(z)}{mv^2} r_n \quad (127)$$

where  $l$  is the step size in  $z$ -direction, such that  $z = nl$ . Values for the initial radius  $r_0$  and the initial slope  $k_0$  of the beam trajectory have to be provided. As well as the initial velocity  $v$  of the particle and the sextupole strength  $g_s(z)$  as a function of  $z$ .

First this algorithm is applied to gain a better understanding of the velocity selection and polarizing properties of the CERN sextupole magnet doublet. Then the trajectories of several hydrogen beam setups are investigated. Finally the algorithm is used to design the layout of the new beam optics using ring apertures.

## 6.4 Velocity Selection of a Sextupole Doublet

The CERN sextupole magnet doublet consists of two magnets 65 mm long with strength  $g_s = 144\,000 \text{ T m}^{-2}$  (calculated from the given values in reference [38]). As a model of  $g_s(z)$  a rectangular function is used which is equal to  $g_s$  at the magnets position and zero otherwise. Boundary effects of the magnets, therefore, are not taken into account.

Figure 30 shows simulated trajectories of hydrogen atoms traversing the CERN magnet doublet for the 4 ground states of hydrogen for one initial velocity and multiple initial angles.

The hydrogen atoms in state  $|1\rangle$  are refocussed onto a point at  $z = 160 \text{ mm}$  by the first magnet. The focal point of the atoms in state  $|2\rangle$  strongly depends on the radius at which they are deflected. For large radii the focal point is close to the focal point for state  $|1\rangle$ , for small radii the deflection becomes weaker and the focal points shifts downstream. Atoms in state  $|3\rangle$  and  $|4\rangle$  are defocussed and removed from the beam.

In the setup the paths of the hydrogen atoms depend on the velocity of the atom. Atoms with larger velocity are deflected less and their focal point is farther downstream than for atoms with small velocity. By increasing the distance between the magnet doublet, atoms of larger velocities are focussed at the position of the aperture. If an aperture of appropriate size is placed at this point, atoms with a certain velocity are selected. By variation of

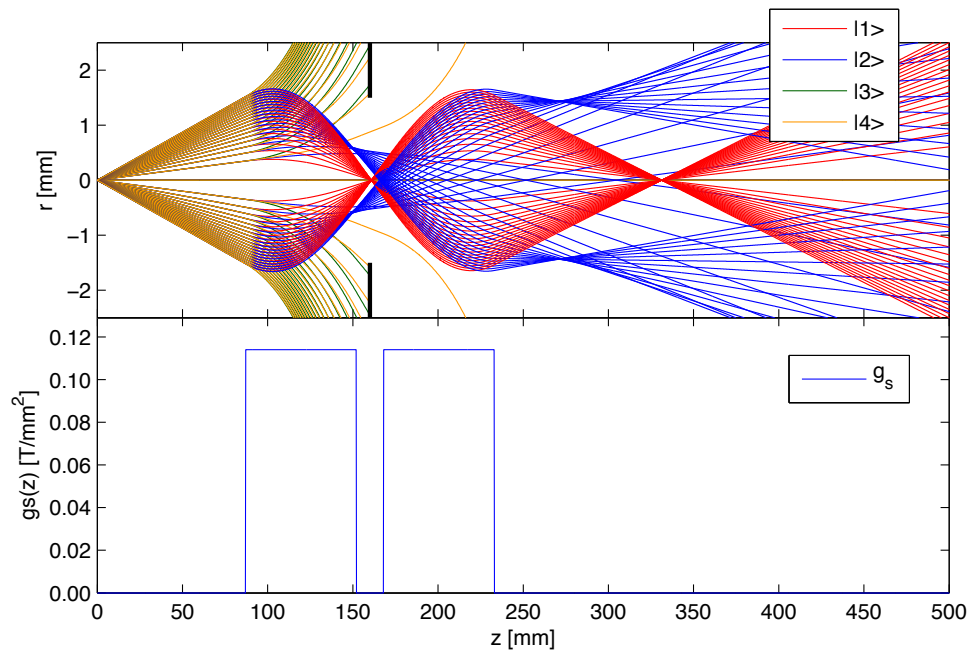
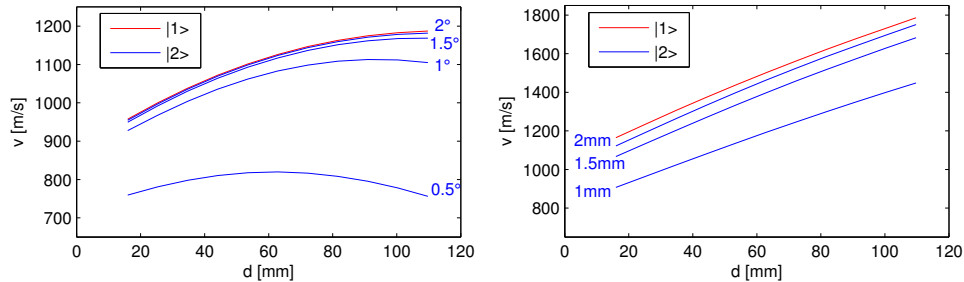


Figure 30: Top: Trajectories of hydrogen atoms in the CERN sextupole doublet. For the initial velocity  $v_i = 937 \text{ m s}^{-1}$  multiple angles are simulated. The aperture with diameter 3 mm at  $z = 160$  mm is indicated in black. The source is placed at position  $z = 0$  mm. Bottom: sextupole strength  $g_s(z)$  of the assembly.

the distance between the magnet doublet, the transmitted velocity can be selected. The width of the transmitted velocity distribution depends on the diameter of the aperture.

Figure 31 shows the results of a simulation to determine the transmitted velocity of the CERN magnet doublet as a function of distance between both magnets for an infinitely small aperture placed in the center between the magnets.



(a) Divergent beam. For a distance of 160 mm between the source and the magnet doublet.

(b) Parallel beam.

Figure 31: Simulation of transmitted velocity as a function of distance between both magnets of the CERN sextupole doublet for a divergent beam (a) and a parallel beam (b). The divergent beam originates from a source 160 mm upstream of the magnet doublet. The simulation assumes an infinitely small aperture. For state  $|1\rangle$  the transmitted velocity depends only on the distance, for state  $|2\rangle$  it depends also on the initial angle of a divergent beam (a) or on the initial radius of a parallel beam (b).

Velocity selection works very well for hydrogen atoms in state  $|1\rangle$ . For atoms in state  $|2\rangle$ , for different initial angles different velocities are allowed to pass through the aperture. Therefore, the width of the transmitted velocity distribution is broader for state  $|2\rangle$  than for state  $|1\rangle$ .

## 6.5 Setup Configurations 2.1 and 2.2

In the setup configurations 2.1 and 2.2 the CERN magnet doublet is applied as velocity selector. The difference between configurations 2.1 and 2.2 is the cavity, which is removed in configuration 2.2. Trajectories of hydrogen atoms in setup 2.1 are shown in figure 32. The trajectories and effects in setup 2.2 are similar, with the positions of the second set of SMI magnets and the QMS detector 560 mm further upstream.

As can be seen in figure 32, the beam is divergent downstream of the CERN magnet doublet until it is refocussed onto the detector by the SMI magnets. Because this refocussing is velocity dependent, the velocity selected by the CERN magnets has to match the velocity for which the SMI magnets

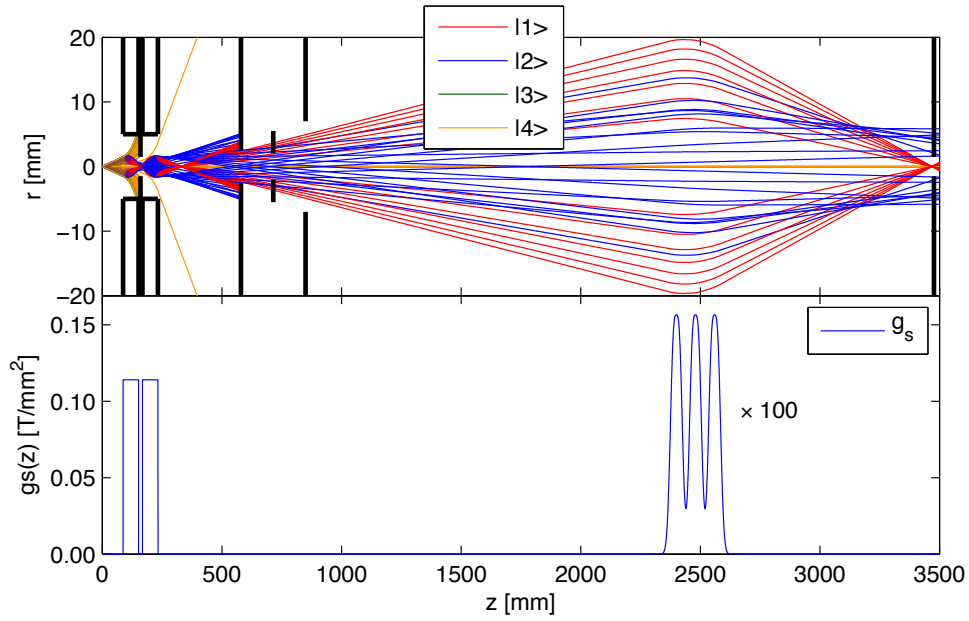


Figure 32: Trajectories in setup configuration 2.1 "permanent magnets" (top) and sextupole strength  $g_s(z)$  (bottom). The beam emerges from the skimmer at  $z = 0$  mm. The sextupole doublet (with an aperture of 3 mm diameter between the two magnets) is centered at  $z = 160$  mm. The chopper position at  $z = 715$  mm is indicated in black. Apertures for differential pumping at  $z = 580$  mm and  $z = 850$  mm are shown in black. And the QMS detector is located at  $z = 3477$  mm. The  $g_s$  of the analysis magnets at  $z = 2480$  mm is amplified by a factor of 100.

focus the beam onto the QMS detector.

A narrow band of velocities is selected for state  $|1\rangle$ , such that most atoms are focussed onto the QMS detector. A broad band of velocities is selected for state  $|2\rangle$  and only a small fraction is focussed onto the sensitive area of the QMS detector, most of the beam is focussed to points in front of, or behind the QMS detector. The transmitted velocities for a beam with initial angle  $\leq 1.2^\circ$  and a distance between the sextupole doublet of  $d = 53.5$  mm is shown in figure 33.

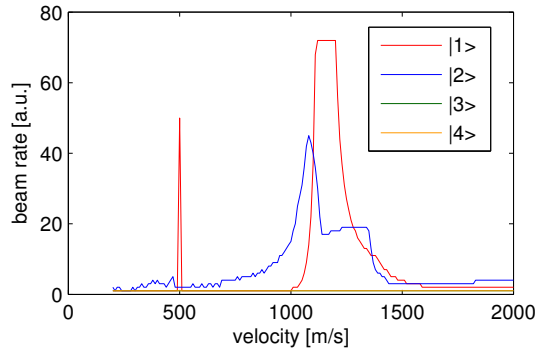


Figure 33: Velocity transmission of the setup configurations 2.1 and 2.2. A beam with initial angle  $\leq 1.2^\circ$  is simulated for a sextupole distance  $d = 53.5$  mm.

As a result the LFS-polarization<sup>12</sup>  $P_{\text{LFS}} = \frac{N_1 - N_2}{N_1 + N_2}$  is large because much more atoms in state  $|1\rangle$  arrive at the detector than atoms in state  $|2\rangle$ .

The fact that the trajectories of the hydrogen atoms in state  $|1\rangle$  are focussed onto the detector, but atoms in state  $|2\rangle$  are not, led to the development of the new beam optics described in the next section.

## 6.6 Principle of New Beam Optics

From equation 112 follows that the deflection of state  $|2\rangle$  depends strongly on the magnetic field. At a field of  $B = B_C$  the force on state  $|2\rangle$  is 71% of the force for state  $|1\rangle$ , at  $B = 3B_C$  the force is already 95% of that on state  $|1\rangle$ .

In the sextupole magnet the radius and the magnetic field are related.

<sup>12</sup>Usually the polarization is defined as  $P = \frac{N_{\text{HFS}} - N_{\text{LFS}}}{N_{\text{HFS}} + N_{\text{LFS}}}$  (where HFS denotes states  $|3\rangle$  and  $|4\rangle$  and LFS denotes states  $|1\rangle$  and  $|2\rangle$ ) and describes the excess of HFS states over LFS states. Here the LFS-polarization  $P_{\text{LFS}} = \frac{N_1 - N_2}{N_1 + N_2}$  describes the excess of states  $|1\rangle$  over states  $|2\rangle$  in the transmitted beam of LFS. For equal statistics of  $\pi$ - and  $\sigma$ -resonances  $P_{\text{LFS}}$  should be close to zero.

For every magnet a characteristic radius

$$r_c = \sqrt{\frac{2B_C}{g_s}} \quad (128)$$

can be calculated (table 9). At this radius the force on state  $|2\rangle$  is 71% lower compared to state  $|1\rangle$ . At  $r = \sqrt{3}r_c$  this factor is already 95%.

The principle of the new apertures is based on blocking the central part of the beam, where the deflection of states  $|1\rangle$  and  $|2\rangle$  are very different. For the parts of the beam that are able to reach the detector, the difference in deflection is smaller than  $\approx 5\%$ . Furthermore, the arrangement of magnets and following from this the trajectories of the atoms are rather symmetric with respect to the plane equidistant from the source and detector.

magnet	strength $g_s$ [T m <sup>-2</sup> ]	radius $r_c$ [mm]
SMI	1600	8.0
CERN	114000	0.94
SC at 350 A	2000	7.1

Table 9: Characteristic radius  $r_c$  for different types of sextupole magnets. SC = superconducting magnet.

## 6.7 Setup Configuration 2.3

The setup configuration 2.3 is designed according to the principles discussed above. Trajectory simulations (figure 34) show that – for the right velocity – the beam is made parallel by the first set of magnets, and focussed onto the detector by the second set of magnets. The velocity at which that happens is slightly different for atoms in state  $|1\rangle$  and state  $|2\rangle$ .

To determine the velocity transmission of the setup, trajectories for 180 angles and 180 velocity values are calculated. They are filled into a histogram if they hit the detector within a diameter of 3 mm. The resulting histogram is shown in figure 35. Only particles within a narrow window of velocities will arrive at the detector. The mean velocity  $v$  and velocity width  $\sigma_v$  for states  $|1\rangle$  and  $|2\rangle$  are:

$$v_1 = 1040.4 \text{ m s}^{-1} \quad v_2 = 974.1 \text{ m s}^{-1} \quad (129)$$

$$\sigma_{v_1} = 13.4 \text{ m s}^{-1} \quad \sigma_{v_2} = 26.3 \text{ m s}^{-1} \quad (130)$$

The LFS-polarization is defined as

$$P_{\text{LFS}} = \frac{N_1 - N_2}{N_1 + N_2} \quad (131)$$

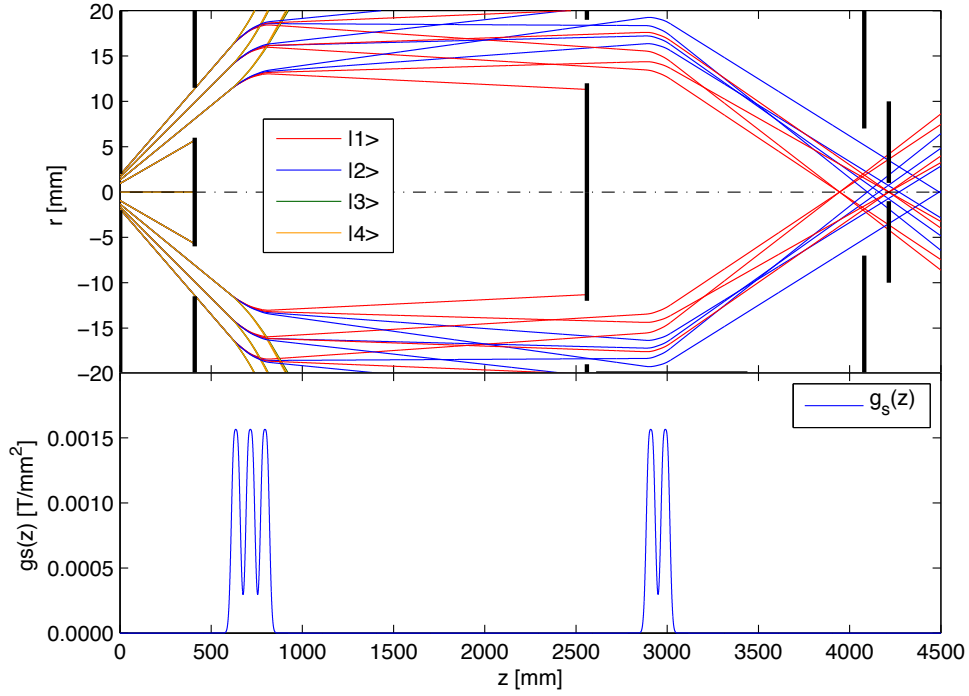


Figure 34: Simulated trajectories in setup configuration 2.3 "ring aperture" (top) and sextupole strength  $g_s(z)$  (bottom). Trajectories for 4 different angles and 2 velocities ( $990 \text{ m s}^{-1}$  and  $1040 \text{ m s}^{-1}$ ) are shown. The beam emerges from the source at position  $z = -80 \text{ mm}$ . The ring aperture 1 with inner diameter 12 mm and outer diameter 23 mm is displayed at  $z = 410 \text{ mm}$  and ring aperture 2 with inner diameter 24 mm and outer diameter 38 mm is displayed at  $z = 2560 \text{ mm}$ . SMI magnets are shown at positions  $z = 635 \text{ mm}$ ,  $715 \text{ mm}$ ,  $795 \text{ mm}$ ,  $2910 \text{ mm}$  and  $2990 \text{ mm}$ . An aperture for differential pumping at position  $z = 4065 \text{ mm}$  is indicated in black. And the QMS detector is located at position  $z = 4215 \text{ mm}$ .

where  $N_1$  and  $N_2$  are the number of atoms in states  $|1\rangle$  and  $|2\rangle$ , respectively. For setup 2.3 the calculated LFS-polarization is:

$$P_{\text{LFS}} = -0.18 \quad (132)$$

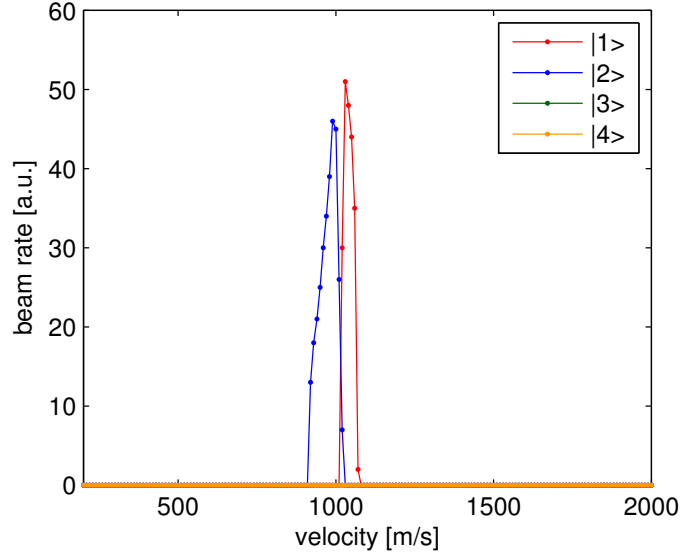


Figure 35: Velocity transmission of ring aperture setup. The mean velocity for state  $|1\rangle$  is  $1040.4 \text{ m s}^{-1}$ . For state  $|2\rangle$  it is  $974.1 \text{ m s}^{-1}$ . State  $|3\rangle$  and  $|4\rangle$  do not reach the detector at all.

## 6.8 Summary of the Trajectory Simulations

The here developed simplified model of the hydrogen beam provided useful insights into the transport of atoms through the setup. As well as into the results of the quantum mechanical effect of the mixing of states  $|1/2, -1/2\rangle$  and  $| - 1/2, 1/2\rangle$  which leads to a drop  $> 5\%$  in the magnetic moment of state  $|2\rangle$  for fields lower than  $3B_C$ .

Trajectory simulations of hydrogen atoms in ground state show that the behavior of states  $|1\rangle$  and  $|2\rangle$ , which are usually called low field seekers, is very different in low magnetic fields (lower than  $3B_C$ ). The simulations further show that, because the states are deflected differently, the LFS-polarization is highly dependent on the position of the detector.

## 7 Resonance Measurements

In this chapter the measurements of both the  $\sigma$ - and  $\pi$ -transition using setup configurations 2.1 and 2.3 are reported.

### 7.1 Line Shape

In the magnetic field of the earth the frequencies of the  $\sigma$ - and  $\pi$ -transition are sufficiently separated to treat each transition in the framework of a 2-level system:

$$\pi : |1\rangle \leftrightarrow |4\rangle \quad (133)$$

$$\sigma : |2\rangle \leftrightarrow |4\rangle \quad (134)$$

The line shape is calculated by solving the optical Bloch equations for each 2-level system. Because of the cosine shaped oscillating magnetic field inside the strip line cavity, the transition probability has two peaks (figure 36). They are symmetric with respect to the central frequency, which is the transition frequency.

Simulations of the line shape have been carried out by C. Sauerzopf [21]. For a given interaction time  $t$ , the transition probability depends on the amplitude of the oscillating magnetic field  $B_0$  and the frequency detune  $\Delta = \nu - \nu_T$ , the difference between microwave frequency  $\nu$  and transition frequency  $\nu_T$ . Figure 37 shows the transition probability as a function of  $B_0$  and  $\Delta$  for a beam with velocity  $v = 1000 \text{ m s}^{-1}$  in a cavity of length  $l = 100 \text{ mm}$  (with an interaction time of  $t = l/v = 100 \text{ }\mu\text{s}$ ).

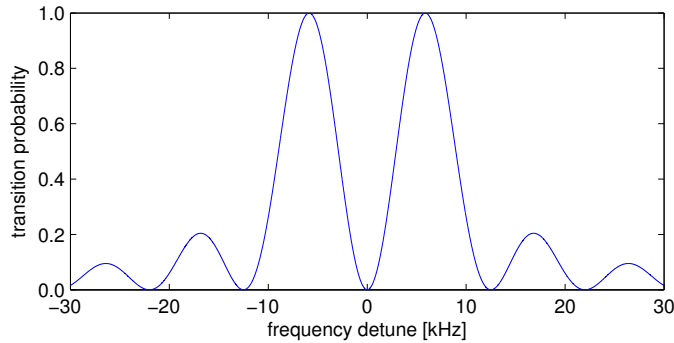


Figure 36: Transition probability of a  $v = 1000 \text{ m s}^{-1}$  beam at an oscillating field amplitude of  $B_0 = 6.0 \times 10^{-7} \text{ T}$  for a cavity of length  $l = 109.5 \text{ mm}$  (the length of the strip line cavity used, see section 3.7).

Because the transition probability depends on the interaction time  $t$ , the line shape is different for different velocity components of the beam. The simulation was carried out for one specific velocity  $v$ . The line shape for

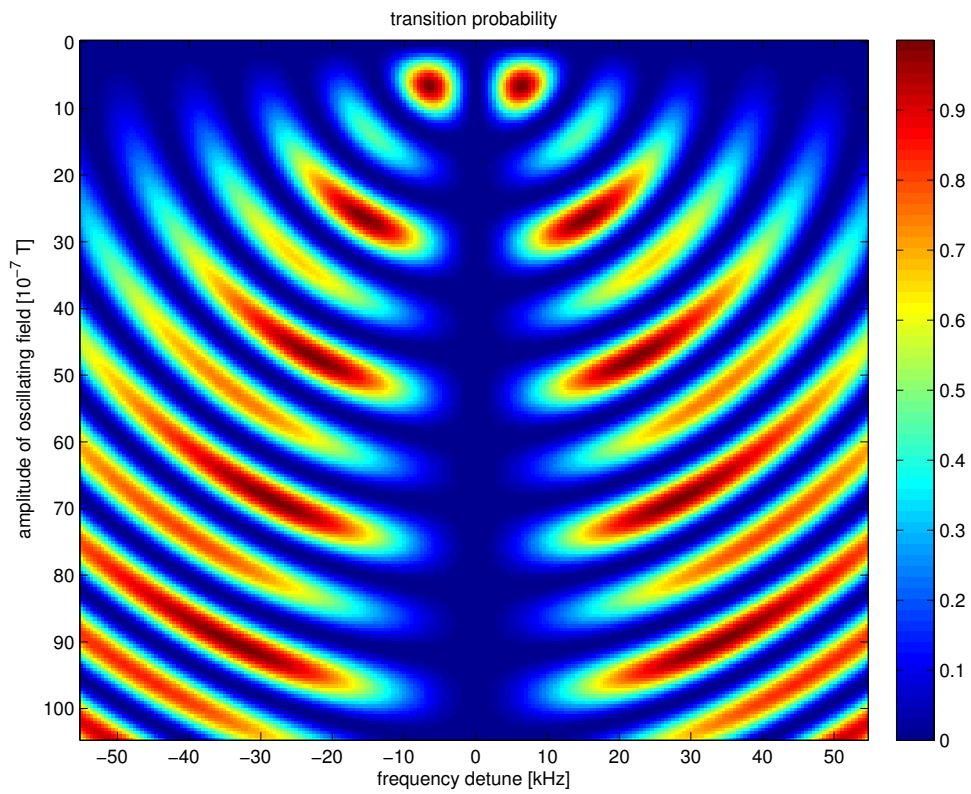


Figure 37: Simulated transition probability as a function of oscillating field amplitude  $B_0$  and frequency detune  $\Delta$  for a beam with velocity  $v = 1000 \text{ m s}^{-1}$  in a cavity of length  $l = 100 \text{ mm}$ .

a different velocity  $v'$  can be calculated by scaling the magnitude of the oscillating field  $B'_0 = B_0 \frac{v'}{v}$  and frequency detune  $\Delta' = \Delta \frac{v'}{v}$ .

The line shape which takes into account a velocity spread is a sum of line shapes for several velocities, calculated as follows: For a given velocity  $v$ , the transition probability at  $B_0$  and  $\Delta$  are determined by 2d spline interpolation<sup>13</sup> on a grid of simulated values. The line shapes for  $n$  velocities  $v - \frac{n}{2} \times dv, v - (\frac{n}{2} + 1) \times dv, \dots, v + \frac{n}{2} \times dv$  are summed with weights according to the binomial factor, as discrete approximation to a gaussian velocity distribution. This results in the transition probability

$$\rho = \rho(v, \sigma_v, B_0, \Delta). \quad (135)$$

To fit the measured data the line shape is shifted by the transition frequency  $\nu_T$  and scaled with the count rate drop  $a$ . A constant baseline rate  $b$  is added:

$$N = b - a \rho(v, \sigma_v, B_0, \Delta - \nu_T). \quad (136)$$

By fitting this line shape to the measured data of beam rate versus microwave frequency, the transition frequency  $\nu_T$ , the mean beam velocity  $v$  and the beam velocity width  $\sigma_v$  are determined.

## 7.2 Measurement Method

The setup is aligned by optical means with the help of a laser beam. A beam of hydrogen atoms is introduced into the setup, the chopper is activated, and the QMS detector is adjusted in the plane perpendicular to the beam such that the rate at the detector is a maximum.

Then microwaves of a certain frequency and amplitude are introduced into the cavity. Two histograms of count rate versus chopper phase are recorded by the software lock-in amplifier for every setting of frequency and amplitude. The recording time for one histogram is set to 30 s. Therefore, the recording time per frequency or amplitude point is 60 s.

First the microwave frequency is scanned at a certain oscillating magnetic field amplitude. Then the frequency is set to the maximal transition probability (minimum count rate) and the amplitude is scanned. After this scan, the amplitude is set to the maximal transition probability and this amplitude setting is used throughout the following measurements.

Then a range of typically 51 frequencies are scanned in random order. The result is a histogram of count rate versus microwave frequency with a total recording time of 3060 s. This scan process is then repeated several times for the  $\sigma$ -transition (see # of repetitions in table 10).

After this process for the  $\sigma$ -transition, the frequency is switched to a range covering the  $\pi$ -transition and one histogram of count rate versus microwave frequency is recorded. Then the frequency is set to one of the peaks

---

<sup>13</sup>The MATLAB function `griddata` with the option 'cubic' was used to perform the two dimensional cubic spline interpolation.

in transition probability (minimum in count rate) and a scan in amplitude is performed. The amplitude is set to the maximal transition probability. Then several histogram of count rate versus microwave frequency are recorded for the  $\pi$ -transition.

An overview of the recorded measurements is provided in table 10.

measurement #	transition	# of frequencies	# of repetitions	beamline
1	$\sigma$	51	14	2.3
2	$\pi$	51	22	2.3
3	$\pi$	41	3	2.1
4	$\sigma$	41	9	2.1
5	$\pi$	41	6	2.1

Table 10: Overview of measurements of the  $\sigma$ - and  $\pi$ -transition frequency. The recording time for one repetition is 3060s for measurements 1 and 2. For measurements 3 to 5 the recording time of one repetition is 2460s.

### 7.3 Analysis of $\pi$ - and $\sigma$ -Resonances in Earths Magnetic Field

The beam rate of one repetition is determined by fitting a positive half-wave of a sine<sup>14</sup> to the histogram of count rate versus chopper phase, as already described in chapter 5. This results in  $n$  estimates for the beam rate, where  $n$  is the number of repetitions. As the beam rate is determined by the fit function, it is not associated with a poisson error. The error of the fit parameter is used instead. For a certain frequency the final beam rate is determined by a weighted mean of the  $n$  beam rate values for the  $n$  repetitions. The error is estimated by the standard deviation of the weighted mean.

#### 7.3.1 Configuration 2.1 "Permanent Magnets"

The beam rate around the  $\sigma$ - and  $\pi$ -transition frequency for configuration 2.1 is shown in figure 38, 39, and 40.

These plots of beam rate versus microwave frequency are fitted with the line shape function discussed above. In table 11 the results of the fit are summarized. The fit results for the velocity of atoms in state  $|1\rangle$  is  $v_1 \approx 1260 \text{ m s}^{-1}$  and of atoms in state  $|2\rangle$  it is  $v_2 \approx 1090 \text{ m s}^{-1}$ . Both are compared to simulated values in section 7.4.

The results in table 11 show large fit errors on the count rate drop  $a$  and oscillating magnetic field amplitude  $B_0$  originating from a strong correlation of these two fit parameters. Therefore, the count rate drop is determined by

<sup>14</sup>The positive half-wave of a sine was used instead of the truncated and convoluted version because both the truncation factor and the width of the gaussian are typically associated with large fit errors.

quantity	$\pi$ -measurement (3)	$\sigma$ -measurement (4)	$\pi$ -measurement (5)	unit
$B_0$	$521 \pm 93$	$319 \pm 500$	$473 \pm 100$	$10^{-7}$ T
$b$	$1232.8 \pm 5.7$	$1229.9 \pm 2.6$	$1177.7 \pm 3.8$	Hz
$\nu_T$	$1\,420\,746\,970 \pm 19$	$1\,420\,405\,897 \pm 41$	$1\,420\,746\,503 \pm 14$	Hz
$a$	$1\,021 \pm 180$	$309 \pm 730$	$1102 \pm 280$	Hz
$\sigma_v$	$71 \pm 18$	$92 \pm 29$	$82 \pm 12$	$\text{m s}^{-1}$
$v$	$1261 \pm 16$	$1094 \pm 44$	$1\,264 \pm 14$	$\text{m s}^{-1}$
SSE	69.9	49.6	84.8	
DOF	35	35	35	
RMSE	1.41	1.19	1.56	

Table 11: Fit results for configuration 2.1 "permanent magnets".

a fit with the magnitude of the oscillating magnetic field  $B_0$  fixed at a value where the transition probability is a maximum ( $B_0 = 6.5 \times 10^{-7}$  T). This is justified, as  $B_0$  has been set to the optimal value after the power scan. The results of the fit with the fixed  $B_0$  are summarized in table 12.

The rates of atoms in state  $|1\rangle$  and  $|2\rangle$  are denoted  $N_1$  and  $N_2$ , respectively.  $N_1$  and  $N_2$  are determined by the count rate drop of the  $\pi$ - and  $\sigma$ -transition, respectively. The results determined by the fit with fixed  $B_0$  are

$$N_1 \approx 807 \text{ Hz} \qquad N_2 \approx 153 \text{ Hz} \qquad (137)$$

quantity	$\pi$ -measurement (3)	$\sigma$ -measurement (4)	$\pi$ -measurement (5)	unit
$b$	$1248.7 \pm 5.2$	$1230.5 \pm 2.5$	$1185.0 \pm 4.7$	Hz
$a$	$830 \pm 12$	$153.2 \pm 5.5$	$783 \pm 10$	Hz
SSE	111	54	141	
DOF	36	36	36	
RMSE	1.76	1.22	1.98	

Table 12: Results of fit with oscillating magnetic field fixed at  $B_0 = 6.5 \times 10^{-7}$  T. For configuration 2.1.

The LFS-polarization then becomes

$$P_{\text{LFS}} = \frac{N_1 - N_2}{N_1 + N_2} = 0.68 \qquad (138)$$

As expected from the simulations in section 6.5 the value is large.

There is a discrepancy, because the sum of  $N_1$  and  $N_2$  is not equal to the baseline rate  $b$  of  $\approx 1220$  Hz. Additional states other than  $|1\rangle$  and  $|2\rangle$  are present in the measured beam at a rate of  $\approx 260$  Hz.

As one can see from table 11, the errors of the estimates for the amplitude of the oscillating magnetic field  $B_0$  and the count rate drop  $a$  are

very large. The aforementioned correlation between these two fit parameters can be avoided by choosing a wider scan range, which covers the side lobes in addition to the two main peaks. Therefore, for future measurements a wider range of frequencies is chosen. As can be seen in the next section on the resonance measurements using the configuration 2.3, the errors of the estimates for  $B_0$  and  $a$  are smaller.

### 7.3.2 Configuration 2.3 "Ring Aperture"

The beam rate versus frequency plots of the  $\sigma$ - and  $\pi$ -transition in the setup configuration 2.3 are shown in figure 41 and 42, respectively.

In table 13 the results of the fit (as discussed above) are summarized. The fit result for the velocities of atoms in state  $|1\rangle$  or  $|2\rangle$  are:

$$v_1 = 1043.7 \pm 7.8 \text{ m s}^{-1} \quad v_2 = 975.3 \pm 6.3 \text{ m s}^{-1} \quad (139)$$

quantity	$\sigma$ -measurement (1)	$\pi$ -measurement (2)	unit
$B_0$	$599 \pm 22$	$515 \pm 37$	$10^{-7} \text{ T}$
$b$	$730.7 \pm 2.0$	$740.3 \pm 2.0$	Hz
$\nu_T$	$1\,420\,406\,019 \pm 29$	$1\,420\,849\,899 \pm 29$	Hz
$a$	$331.3 \pm 4.3$	$390 \pm 18$	Hz
$v$	$975.3 \pm 6.3$	$1\,043.7 \pm 7.8$	$\text{m s}^{-1}$
SSE	62.9	98.9	
DOF	46	46	
RMSE	1.17	1.47	

Table 13: Fit results for configuration 2.3 "ring aperture".

The error on the count rate drop  $a$  is small, therefore  $a$  is used as estimate for the rates  $N_1$  and  $N_2$ . The LFS-polarization becomes

$$P_{\text{LFS}} = \frac{N_1 - N_2}{N_1 + N_2} = 0.08 \quad (140)$$

For configuration 2.3 the sum of  $N_1$  and  $N_2$  is consistent with the baseline rate  $b$  within one standard deviation.

In comparison with the configuration 2.1 the rate of atoms in state  $|2\rangle$  is larger by a factor of 2. However, the rate of atoms in state  $|1\rangle$  is smaller by a factor of 2. In configuration 2.3 the LFS-polarization is close to 0, which provides beams of almost equal intensity. This enables the measurement of both the  $\sigma$ - and the  $\pi$ -transition with comparable statistics.

### 7.3.3 Comparison of Beam Rate and Total Count Rate

A fit to the total count rate is shown in figure 43 for measurement # 1. As the total rate is the number of counts in the measurement interval of 60 s, poisson errors are used.

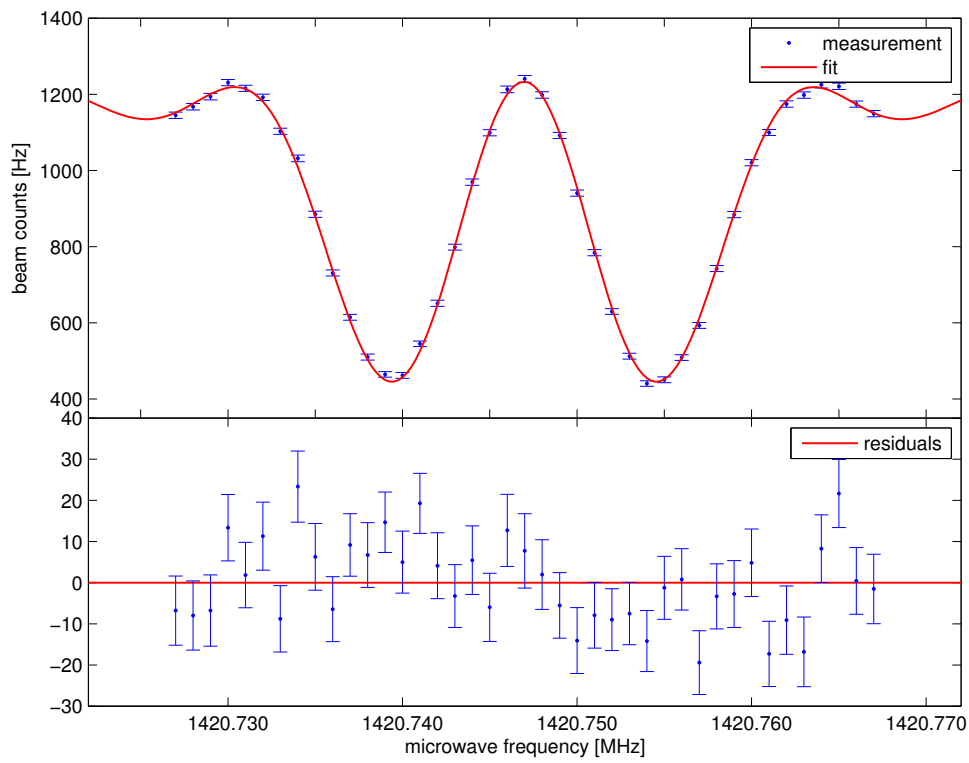


Figure 38: Top: measurements of beam rate versus microwave frequency at the  $\pi$ -resonance in setup configuration 2.1 ("permanent magnets"). Bottom: residuals.

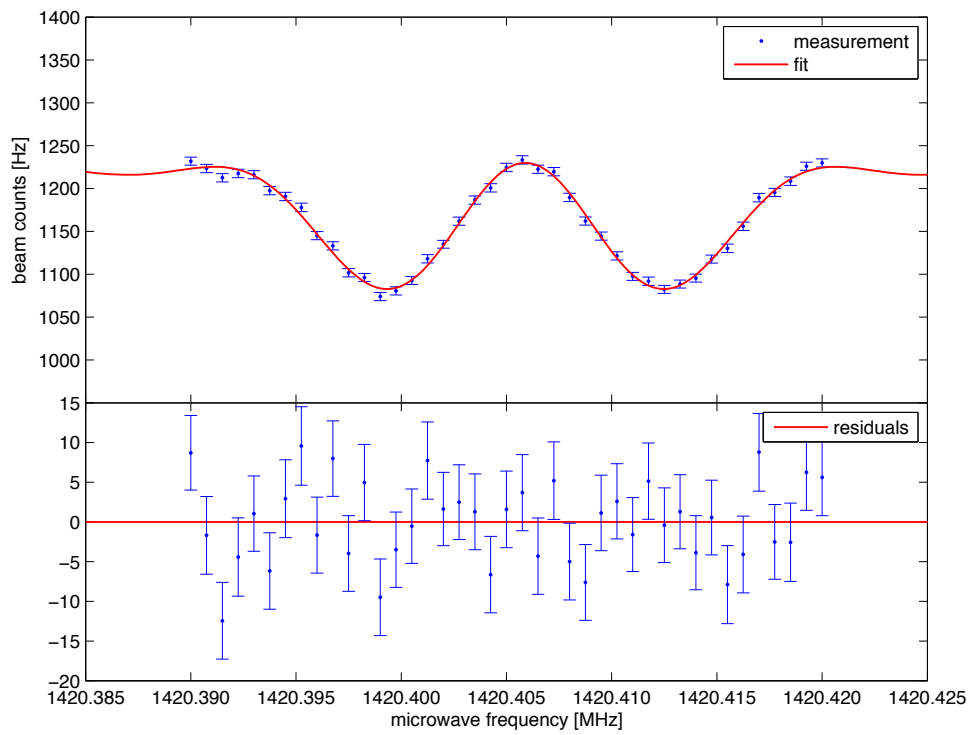


Figure 39: Top: measurements of beam rate versus microwave frequency at the  $\sigma$ -resonance in setup configuration 2.1 ("permanent magnets"). Bottom: residuals.

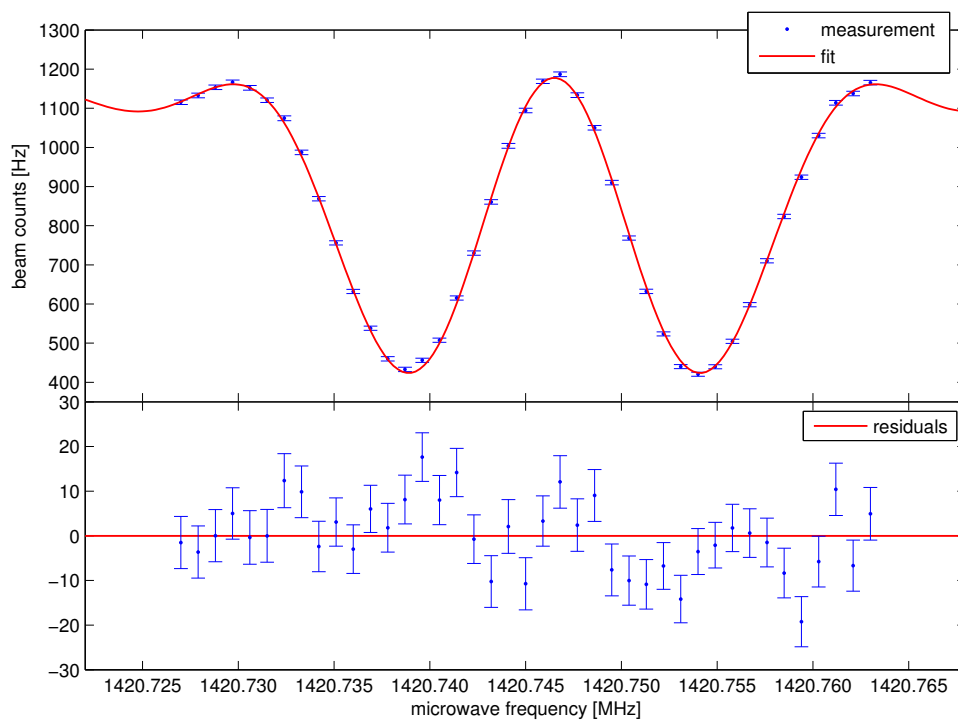


Figure 40: Top: measurements of beam rate versus microwave frequency at the  $\pi$ -resonance in setup configuration 2.1 ("permanent magnets"). Bottom: residuals.

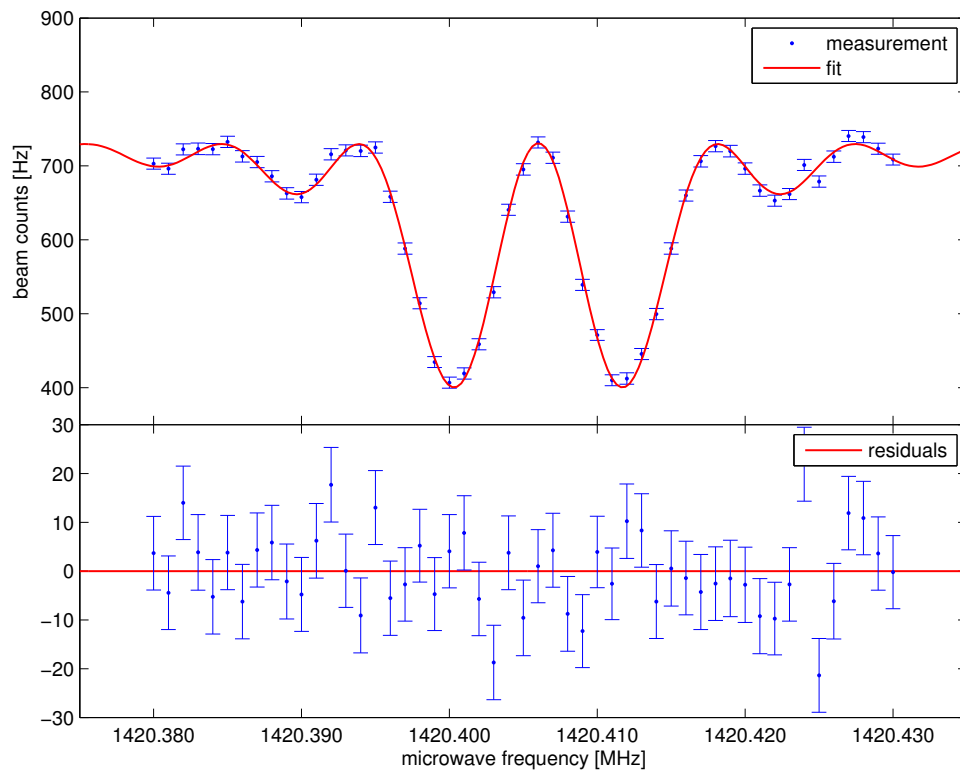


Figure 41: Top: measurements of beam rate versus microwave frequency at the  $\sigma$ -resonance in setup configuration 2.3 ("ring aperture"). Bottom: residuals.

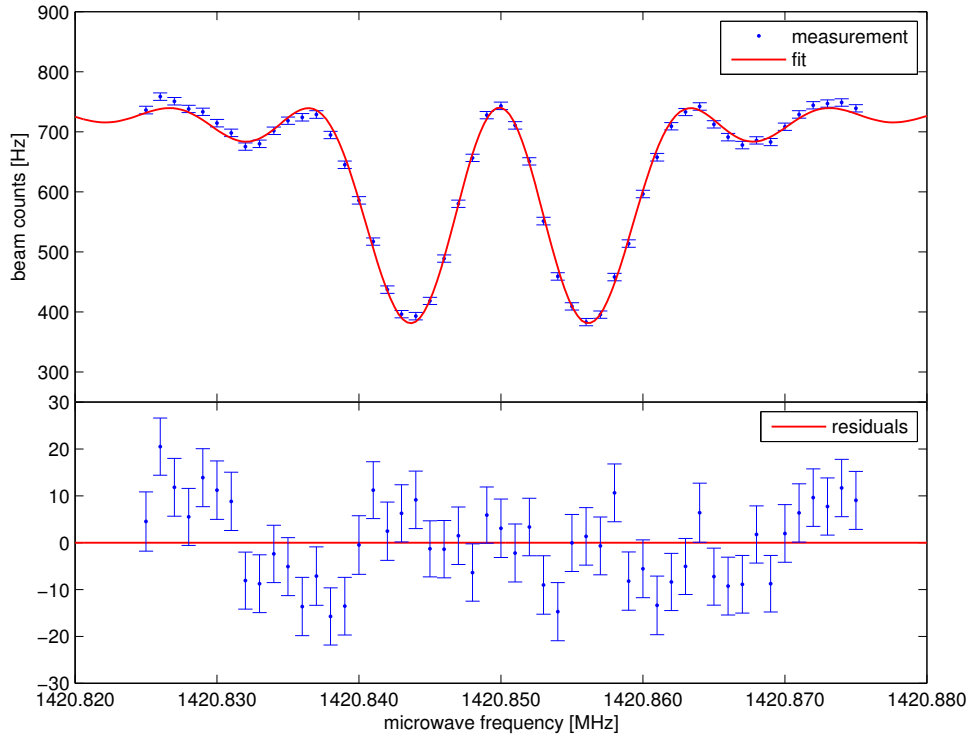


Figure 42: Top: measurements of beam rate versus microwave frequency at the  $\pi$ -resonance in setup configuration 2.3 ("ring aperture"). Bottom: residuals. The remaining structure in the residuals is likely caused by fluctuations of earth's magnetic field. As the  $\pi$  transition frequency is very sensitive to shifts in the magnetic field, this leads to a smearing of the resonance structure. The smearing would lead to negative residuals in the center and positive residuals at the fringes, as observed. Since the cavity was not shielded, other sources of varying magnetic field are also a possible cause.

The scatter in the total rate signal is larger compared to the beam rate signal, and the higher order peaks are barely visible. The fit result for the transition frequency  $\nu_T$  is:

$$\nu_T = 1\,420\,406\,096 \pm 133 \text{ Hz} \quad (141)$$

The error in the transition frequency is much larger than the one determined by the beam rate signal.

A varying background rate is the most probable cause for the degradation of the total rate signal. The varying background rate leads to the large scatter in the total rate. In the signal of the beam rate this effect is entirely absent because of the lock-in detection scheme.

An overview of the other fit parameters is shown in table 14.

fit parameter	beam rate fit	total rate fit	unit
$B_0$	$599 \pm 22$	$634 \pm 140$	$10^{-7} \text{ T}$
$\nu_T$	$1\,420\,406\,019 \pm 29$	$1\,420\,406\,096 \pm 133$	Hz
$a$	$331.3 \pm 4.3$	$378 \pm 58$	Hz
$v$	$975.3 \pm 6.3$	$943 \pm 39$	$\text{m s}^{-1}$
SSE	62.9	19.2	
DOF	46	45	
RMSE	1.17	0.65	

Table 14: Comparison of fit values for fits of beam rate and total rate for measurement #1

The situation was different in previous measurements by M. Diermeier [26] where the total count rate resulted in better fit errors. However, the configuration featured the cold bore of the superconducting sextupole and omitted the aperture upstream of the QMS detector. Therefore, the transmitted hydrogen atoms accumulated in the QMS chamber and were detected as background rate, while the chopped signal of the hydrogen atoms in the beam was relatively small.

## 7.4 Comparison with Simulation

The fit result for velocities of the atoms in states  $|1\rangle$  and  $|2\rangle$  in setup configuration 2.1 is

$$v_1 = 1263 \pm 16 \text{ m s}^{-1} \quad v_2 = 1094 \pm 44 \text{ m s}^{-1} \quad (142)$$

They are within the simulated values for a divergent and parallel beam at a CERN magnet distance of  $d = 44 \text{ mm}$ :

$$v_{1,\text{sim}} = 1072 - 1373 \text{ m s}^{-1} \quad v_{2,\text{sim}} = 1064 - 1269 \text{ m s}^{-1} \quad (143)$$

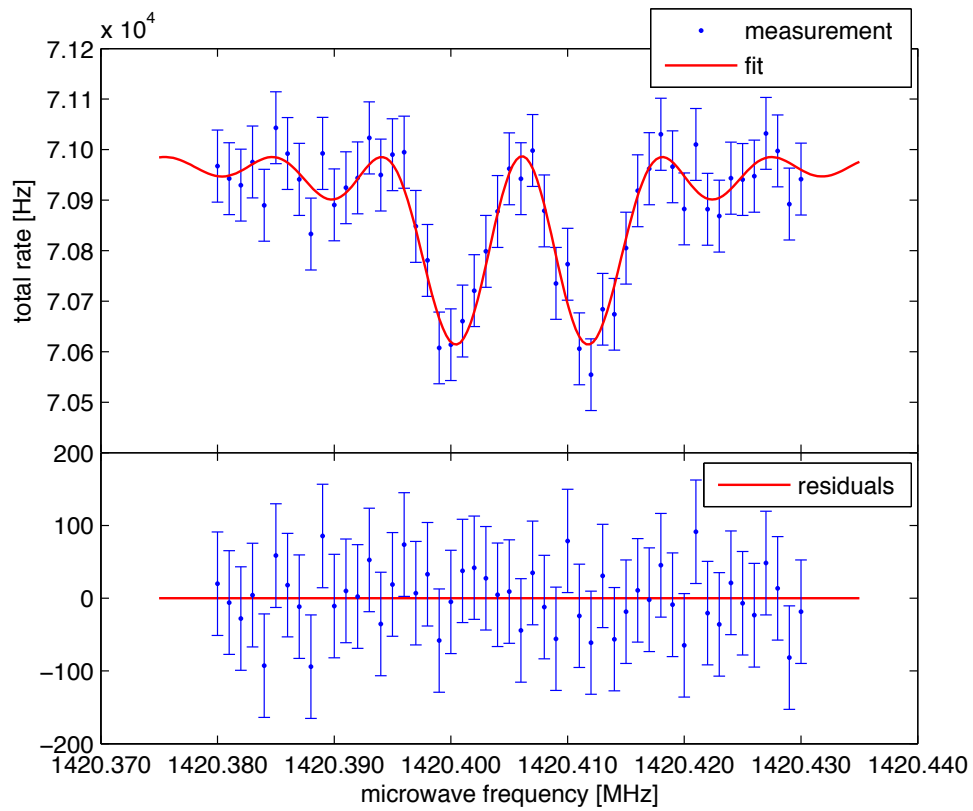


Figure 43: Top: measurements of total rate versus microwave frequency at the  $\sigma$ -resonance in setup configuration 2.3 ("ring aperture"). Bottom: residuals.

The measured LFS-polarization is  $P_{\text{LFS}} = 0.68$ . This large value is expected from the simulations of the transmitted velocities in the CERN magnet doublet (see discussion in section 6.5).

For setup configuration 2.3 the fit results for the velocities of the  $|1\rangle$  and the  $|2\rangle$  component are

$$v_1 = 1043.7 \pm 7.8 \text{ m s}^{-1} \quad v_2 = 975.3 \pm 6.3 \text{ m s}^{-1} \quad (144)$$

They agree very well with the simulated values of

$$v_{1,\text{sim}} = 1040.4 \text{ m s}^{-1} \quad v_{2,\text{sim}} = 974.1 \text{ m s}^{-1} \quad (145)$$

The LFS-polarization in setup configuration 2.3 is measured to be  $P_{\text{LFS}} = 0.08$  while the simulation value is  $P_{\text{LFS}} = -0.18$ . This small discrepancy can be explained if the diameter of the sensitive area of the QMS detector is effectively smaller than  $d = 3 \text{ mm}$ , which was used in the simulation.

## 7.5 Comparison with Time of Flight Velocity Measurements

A time-of-flight (TOF) analysis is carried out for a frequency where only one beam component is present. The second beam component is removed by the transition to state  $|4\rangle$  in the microwave cavity and the subsequent sextupole magnet. The method for the velocity measurement is the same as used to characterize the CERN sextupole doublet and is described in chapter 5.

For configuration 2.1: The frequency of the  $\sigma$ -transition with the lowest count rate is selected and taken as data point for the TOF analysis of the state  $|1\rangle$  beam. Equally, the frequency of the  $\pi$ -transition with the lowest count rate is selected as data point for a TOF analysis of the state  $|2\rangle$  beam.

For configuration 2.3: In addition a dedicated measurement with high statistics is performed, which enables the reconstruction of both the mean velocity and the velocity width.

The results of the TOF analysis for configuration 2.1 are:

$$v_1 = 1316 \pm 4 \text{ m s}^{-1} \quad v_2 = 1241 \pm 19 \text{ m s}^{-1} \quad (146)$$

The results of the TOF analysis for configuration 2.3 are:

$$v_1 = 1074 \pm 15 \text{ m s}^{-1} \quad v_2 = 997 \pm 12 \text{ m s}^{-1} \quad (147)$$

and the result of the dedicated measurement:

$$v_1 = 1069 \pm 12 \text{ m s}^{-1} \quad v_2 = 1008 \pm 11 \text{ m s}^{-1} \quad (148)$$

$$\sigma_{v_1} = 32 \pm 8 \text{ m s}^{-1} \quad \sigma_{v_2} = 44 \pm 6 \text{ m s}^{-1} \quad (149)$$

In comparison with the velocity determined by the fit of the resonance line shape, the velocities measured with the time-of-flight method are larger by 2-3% for configuration 2.3 and 4-13% for configuration 2.1.

## 7.6 Result

Combining the measurements of the  $\sigma$ - and the  $\pi$ -transition of the ground state hyperfine splitting, the zero-field hyperfine transition frequency  $\nu_0$  and the amplitude of the static magnetic field can be calculated:

$$\nu_0 = \frac{\mu'^2}{\mu^2 + \mu'^2} (2\nu_\pi - \nu_\sigma) \pm \frac{\mu^2}{\mu^2 + \mu'^2} \sqrt{\nu_\sigma^2 + 4\frac{\mu'^2}{\mu^2} (\nu_\sigma - \nu_\pi) \nu_\pi} \quad (150)$$

$$B = \frac{h}{\mu} \left( \nu_\pi - \frac{\nu_\sigma}{2} - \frac{\nu_0}{2} \right) \quad (151)$$

For setup configuration 2.1 the result is:

$$\nu_0 = 1\,420\,405\,732 \pm 41 \text{ Hz} \quad (152)$$

$$B = 24.3669 \pm 0.0025 \text{ } \mu\text{T} \quad (153)$$

with a deviation from the literature value of  $\nu_0$  [6] of:

$$\nu_0 - \nu_{0,\text{lit}} = -19 \pm 41 \text{ Hz} \quad (154)$$

For setup configuration 2.3 the result is:

$$\nu_0 = 1\,420\,405\,740 \pm 29 \text{ Hz} \quad (155)$$

$$B = 31.7357 \pm 0.0025 \text{ } \mu\text{T} \quad (156)$$

with a deviation from the literature value of  $\nu_0$  [6] of:

$$\nu_0 - \nu_{0,\text{lit}} = -12 \pm 29 \text{ Hz} \quad (157)$$

From the comparison of both measurements follows that the magnitude of earths magnetic field shifted from 24.367  $\mu\text{T}$  to 31.736  $\mu\text{T}$  over the course of 64 days between the measurements. This change of earths magnetic field is confirmed by the measurements of a flux-gate magnetometer positioned close to the cavity.

The errors of the quantities entering equation 150 are summarized in table 15 and the error budget of the zero-field transition frequency is summarized in table 16 (for the measurement with setup configuration 2.3).

The zero-field hyperfine transition frequency has been determined with a relative accuracy of

$$\frac{\sigma_{\nu_0}}{\nu_0} = 2.0 \times 10^{-8} \quad (158)$$

Note that this is the result of a single measurement with a recording time of 30.6 hours. The measurement was carried out in the (time varying) magnetic field of the earth. However, small variations of the earths magnetic field during the recording did not influence the result at the presented level of accuracy. The result can be improved by controlling the magnetic field and by the statistics of multiple measurements.

quantity	symbol	relative error of quantity
$\pi$ -transition frequency	$\nu_\pi$	$2.0 \times 10^{-8}$
$\sigma$ -transition frequency	$\nu_\sigma$	$2.0 \times 10^{-8}$
magnetic moment	$\mu$	$6.1 \times 10^{-9}$
magnetic moment	$\mu'$	$6.1 \times 10^{-9}$

Table 15: Relative errors of quantities entering the zero-field transition frequency reconstruction (see equation 150).

quantity	relative error of $\nu_0$
$\pi$ -transition frequency	$2.6 \times 10^{-11}$
$\sigma$ -transition frequency	$2.0 \times 10^{-8}$
magnetic moment $\mu$	$2.4 \times 10^{-15}$
magnetic moment $\mu'$	$2.4 \times 10^{-15}$
total	$2.0 \times 10^{-8}$

Table 16: Relative error of the zero-field transition frequency  $\nu_0$  due to the quantities in the left column. The total error is determined by gaussian error propagation.

## 8 Conclusion

Work has been carried out to prepare a spectroscopy apparatus for simultaneous measurement of the  $\sigma$ - and  $\pi$ -transition frequency of antihydrogen atoms in ground state. The apparatus, equipped with a new strip line cavity, has been tested with a beam of hydrogen atoms in earths magnetic field:

Nine permanent sextupole magnets have been built and assembled at SMI. A 3-d positioning stage for recording field maps has been designed and built. The analysis of the recorded field maps showed the high quality of the sextupole magnetic field, and an analytic function suited to describe its strength  $g_s(z)$  has been found. Two configurations have been compared and one of them has been selected to replace the superconducting magnet in the hydrogen beam setup.

The velocity selection properties of a sextupole doublet has been investigated. A beam of hydrogen atoms with Maxwell-Boltzmann distributed velocities has been introduced and the velocities of transmitted atoms have been measured by time-of-flight analysis. The velocity distribution of the transmitted hydrogen atoms is of gaussian shape. The mean velocity depends on the distance between the sextupole doublet. It has been shown that the velocity can be selected within a window of  $1200 \text{ m s}^{-1}$  to  $1600 \text{ m s}^{-1}$  by adjusting the distance between the sextupole doublet.

A simple model of the hydrogen beam has been created and numerical simulations of hydrogen atoms in the spectroscopy apparatus have been carried out. The simulations of the transmitted velocities of the permanent sextupole doublet assembly showed a good agreement with the time-of-flight measurements. They revealed a very different behavior of atoms in state  $|1\rangle$  and  $|2\rangle$  for magnetic fields lower than  $B_C = 0.05 \text{ T}$ . This is because the magnetic moment of atoms in state  $|2\rangle$  is not constant.

The simulations of trajectories in the spectroscopy apparatus and simulations of the transmitted velocity distribution led to the development of new beam optics. These are based on the blocking of the central part of the beam and have been realized using ring apertures. The new beam optics enable the measurement of both  $\sigma$ - and  $\pi$ -transitions with similar measurement time and statistics.

An extremely good agreement between the simulated velocities and the velocities determined by fits of the line shape has been found for the setup employing the new beam optics.

Measurements of the  $\sigma$ - and  $\pi$ -transitions in earths magnetic field have been carried out for both setup configurations. It has been shown that the velocity determined by the line shape of the transition is in agreement with the time-of-flight measurement of the velocity of both beam components. Further it has been shown that the zero-field transition frequency  $\nu_0$  can be determined with a relative accuracy of  $2.0 \times 10^{-8}$  in a single measurement lasting 30.6 hours by making use of the new beam optics.

In the future a controlled magnetic field in the area of the strip line cavity will be provided by the installation of McKeehan coils within a mu-metal shielding. It is also planned to perform long-term measurements to search for sidereal variations or drifts in  $\nu_0$ .

## 9 Appendix A: Physical Constants and Symbol Definitions

With exception of  $\nu_0$ , which is taken from [6], the values of the physical quantities used are taken from CODATA-2014 [54].

The values of  $Ry$ ,  $m$ ,  $\mu$ ,  $\mu'$ , and  $B_C$  are calculated according to the given formulas using values from CODATA-2014 and  $\nu_0$  from [6]. Their errors are determined using gaussian error propagation.

Quantity	Symbol	Value	Unit
speed of light	$c$	299 792 458 (exact)	m s <sup>-1</sup>
magnetic constant	$\mu_0$	$4\pi \times 10^{-7}$ (exact)	N A <sup>-2</sup>
electric constant $1/\mu_0 c^2$	$\epsilon_0$	$8.854\,187\,817\dots \times 10^{-12}$	F m <sup>-1</sup>
planck constant	$\hbar$	$6.582\,119\,514(40) \times 10^{-16}$	eV s
elementary charge	$e$	$1.602\,176\,6208(98) \times 10^{-19}$	C
bohr magneton $e\hbar/2m_e$	$\mu_B$	$5.788\,381\,8012(26) \times 10^{-5}$	eV T <sup>-1</sup>
fine structure constant $e^2/4\pi\epsilon_0\hbar c$	$\alpha$	$7.297\,352\,5664(17) \times 10^{-3}$	
Rydberg constant $m_e c^2 \alpha^2 / 2$	$Ry_\infty$	13.605 693 009(84)	eV
hydrogen Rydberg constant $Ry = \frac{m_p}{m_e + m_p} Ry_\infty$	$Ry$	13.598 287 150(84)	eV
electron mass	$m_e$	0.510 998 9461(31)	MeV
proton mass	$m_p$	938.272 0813(58)	MeV
reduced mass $m = \frac{m_e m_p}{m_e + m_p}$	$m$	0.510 720 7989(31)	MeV
electron g-factor	$g_e$	-2.002 319 304 361 82(52)	
proton g-factor	$g_p$	5.585 694 702(17)	
magnetic moment $\mu = -\frac{1}{2}(g_e + g_p \frac{m_e}{m_p})\mu_B$	$\mu$	$5.786\,289\,9956(26) \times 10^{-5}$	eV T <sup>-1</sup>
magnetic moment $\mu' = -\frac{1}{2}(g_e - g_p \frac{m_e}{m_p})\mu_B$	$\mu'$	$5.803\,898\,6259(26) \times 10^{-5}$	eV T <sup>-1</sup>
hydrogen hyperfine frequency	$\nu_0$	1 420 405 751.768(2)	Hz
magnetic field $B_C = \frac{2\pi\hbar\nu_0}{2\mu'}$	$B_C$	0.050 606 725 87(32)	T

Table 17: CODATA-2014 values and derived quantities used in this work.



## References

- [1] R. Bluhm, V.A. Kostelecky, and N. Russell, *CPT and Lorentz Tests in Hydrogen and Antihydrogen*, Physical Review Letters **82**, 2254 (1999).
- [2] V.A. Kostelecky, and A. Vargas, *Lorentz and CPT Tests with Hydrogen, Antihydrogen, and Related Systems*, Physical Review D **92** 056002 (2015).
- [3] S. Ulmer et al., *High-precision comparison of the antiproton-to-proton charge-to-mass ratio*, Nature **524**, 196–199 (2015).
- [4] ATRAP Collaboration, *One-Particle Measurement of the Antiproton Magnetic Moment*, Physical Review Letters **110**, 130801 (2013).
- [5] C. Parthey et al., *Improved Measurement of the Hydrogen 1S–2S Transition Frequency*, Physical Review Letters **107**, 203001 (2011).
- [6] H. Hellwig, R. F. C. Vessot, M. W. Levine, P. W. Zitzewitz, D. W. Allan, and D. J. Glaze, *Measurement of the Unperturbed Hydrogen Hyperfine Transition Frequency*, IEEE Transactions on Instrumentation and Measurement **19**, 200–209 (1970).
- [7] G.Baur et al., *Production of Antihydrogen*, Physics Letters B **368**, 251–258 (1996).
- [8] S. Maury, *The antiproton decelerator (AD)*, CERN/PS 99-50 (1999).
- [9] M. Amoretti et al., *Production and detection of cold antihydrogen atoms*, Nature **419**, 456–459 (2002).
- [10] G. Gabrielse et al., *Background-Free Observation of Cold Antihydrogen with Field-Ionization Analysis of Its States*, Physical Review Letters **89**, 213401 (2002).
- [11] G. B. Andresen et al., *Trapped antihydrogen*, Nature **468**, 673–676 (2010).
- [12] G. Gabrielse et al., *Trapped Antihydrogen in Its Ground State*, Physical Review Letters **108**, 113002 (2012).
- [13] E. Widmann et al., *Measurement of the antihydrogen hyperfine structure*, Letter of Intent, CERN-SPSC-2003-009, CERN, Geneva, Switzerland (2003).
- [14] E. Widmann, R. Hayano, M. Hori, T. Yamazaki, *Measurement of the hyperfine structure of antihydrogen*, Nuclear Instruments and Methods in Physics Research Section B **214**, 31–34 (2004).

- [15] ASACUSA Collaboration, *Proposal*, CERN-SPSC 2005-002 – P307 Add. 1 (2005).
- [16] Y. Enomoto et al., *Synthesis of Cold Antihydrogen in a Cusp Trap*, Physical Review Letters **105** 243401 (2010).
- [17] N. Kuroda et al., *A Source of Antihydrogen for in-Flight Hyperfine Spectroscopy*, Nature Communications **5**, 3089 (2014).
- [18] I. I. Rabi, S. Millman, P. Kusch, and J. R. Zacharias, *The Molecular Beam Resonance Method for Measuring Nuclear Magnetic Moments*, Physical Review **55**, 526–535 (1939).
- [19] C. Malbrunot et al., *Spectroscopy apparatus for the measurement of the hyperfine structure of antihydrogen*, Hyperfine Interactions **228** 61–66 (2014).
- [20] S. Federmann, *A Spin-Flip Cavity for Microwave Spectroscopy of Antihydrogen*, PhD Thesis, University of Vienna, Vienna (2012).
- [21] C. Sauerzopf, *The ASACUSA Antihydrogen Detector: Development and Data Analysis*, PhD Thesis, Vienna University of Technology, Vienna, (2016).
- [22] C. Sauerzopf, *Annihilation detector for an in-beam spectroscopy apparatus to measure the ground state hyperfine splitting of antihydrogen*, Nuclear Instruments and Methods A (2016).  
<http://dx.doi.org/10.1016/j.nima.2016.06.023>
- [23] M. Diermaier et al., *An atomic hydrogen beam to test ASACUSA’s apparatus for antihydrogen spectroscopy*, Hyperfine Interactions **233**, 35–40 (2015).
- [24] M. Diermaier, *Design and construction of a monoatomic hydrogen beam*, MSc Thesis, University of Vienna, Vienna (2012).
- [25] M. Diermaier et al., *In-beam measurement of the hydrogen hyperfine splitting – towards antihydrogen spectroscopy*, arXiv:1610.06392 (2016).
- [26] M. Diermaier, *Determination of the Hydrogen Ground-State Hyperfine Splitting in a Beam and Perspectives for Antihydrogen*, PhD Thesis, Vienna University of Technology, Vienna (2016).
- [27] E. Schrödinger, *Quantisierung als Eigenwertproblem*, Annalen der Physik **79**, 361–376; **79**, 489–527; **80**, 437–490; **81**, 109–139 (1926).
- [28] E. Schrödinger, *Über das Verhältnis der Heisenberg-Born-Jordanschen Quantenmechanik zu der meinen*, Annalen der Physik **79**, 734–756 (1926).

- [29] P. A. M. Dirac, *The Quantum Theory of the Electron*, Proceedings of the Royal Society A **117**, 610–624 (1928).
- [30] P. A. M. Dirac, *The Quantum Theory of the Electron. Part II*, Proceedings of the Royal Society A **118**, 351–361 (1928).
- [31] H. A. Bethe, *The Electromagnetic Shift of Energy Levels*, Physical Review **72**, 339–341 (1947).
- [32] R. P. Feynman, *Mathematical Formulation of the Quantum Theory of Electromagnetic Interaction*, Physical Review **80**, 440–457 (1950).
- [33] F. Dyson, *Dyson Quantenfeldtheorie*, Springer Berlin Heidelberg (2014).
- [34] E. Fermi, *Über die magnetischen Momente der Atomkerne*, Zeitschrift für Physik **60**, 320–333 (1930).
- [35] R. P. Feynman, R. Leighton, and M. Sands, *The Feynman Lectures on Physics*, Volume II, Basic Books (2011).
- [36] I. I. Rabi, *Space Quantization in a Gyating Magnetic Field*, Physical Review **51**, 652 (1937).
- [37] I. I. Rabi, J. M. B. Kellogg, and J. R. Zacharias, *The Magnetic Moment of the Proton*, Physical Review **46**, 157–163 (1934).
- [38] P. A. Thonet, *Use of Permanent Magnets in Multiple Projects at CERN*, IEEE Transactions on Applied Superconductivity **26**, 4101404 (2016).
- [39] M. Wolf, *Lock-in based detection scheme for a hydrogen beam*, MSc Thesis, University of Vienna, Vienna (2012).
- [40] K. Halbach, *Design of permanent multipole magnets with oriented rare earth cobalt material*, Nuclear Instruments and Methods **169**, 1–10 (1980).
- [41] K. Halbach, *Physical and optical properties of rare earth cobalt magnets*, Nuclear Instruments and Methods **187**, 109–117 (1981).
- [42] K. Halbach, *Perturbation effects in segmented rare earth cobalt multipole magnets*, Nuclear Instruments and Methods **198**, 213–215 (1982).
- [43] P. Blümler, and F. Casanova *Hardware Developments: Halbach Magnet Arrays*, In: New Developments in NMR No. 5, Mobile NMR and MRI: Developments and Applications, Edited by Michael L. Johns, Einar O. Fridjonsson, Sarah J. Vogt, and Agnes Haber, The Royal Society of Chemistry, (2016).
- [44] M. Fleck, *Design of a permanent Halbach sextupole magnet*, Projektarbeit, Vienna University of Technology, Vienna, 2015.

- [45] supermagnete.ch, *Data sheet article Q-50-15-15-N*, [https://www.supermagnete.ch/eng/data\\_sheet\\_Q-50-15-15-N.pdf](https://www.supermagnete.ch/eng/data_sheet_Q-50-15-15-N.pdf).
- [46] Nanotec, *Data sheet: Stepping motor ST2018S0604-A*, <http://de.nanotec.com/produkte/171-st2018-schrittmotor-nema-8/>.
- [47] Arduino, *Data sheet: Arduino Motor Shield*, <https://www.arduino.cc/en/Main/ArduinoMotorShieldR3>.
- [48] Arduino, *Data sheet: Arduino Leonardo*, <https://www.arduino.cc/en/Main/ArduinoBoardLeonardo>.
- [49] Hirst Magnetic Instruments Ltd., *Data sheet: Hirst GM 08 Gaussmeter*, [http://www.hirst-magnetics.com/instruments/gm08\\_p1.shtml](http://www.hirst-magnetics.com/instruments/gm08_p1.shtml).
- [50] Adafruit, *Data sheet: Adafruit ADS1115*, <https://www.adafruit.com/product/1085>.
- [51] B. P. Welford, *Note on a method for calculating corrected sums of squares and products*, *Technometrics* **4**, 419–420 (1962).
- [52] M. Huzan, *CERN Summer Student Programme at the H-Beam, ASACUSA*, Summer Student Report, CERN (2016). <http://cds.cern.ch/record/2217860>
- [53] C. B. Jepsen, *Work Project Report by C. B. Jepsen*, Summer Student Report, CERN (2014). <http://cds.cern.ch/record/1752579>
- [54] Peter J. Mohr, David B. Newell, and Barry N. Taylor, *CODATA recommended values of the fundamental physical constants: 2014*, *REVIEWS OF MODERN PHYSICS*, VOLUME 88, 2016.
- [55] Essen, L., Donaldson, R. W., Bangham, M. J., and Hope, E. G., *Frequency of the Hydrogen Maser*, *Nature*, 229, 110–111 (1971).
- [56] N. F. Ramsey, *A Molecular Beam Resonance Method with Separated Oscillating Fields*, *Physical Review* **78**, 695 (1950).
- [57] N. F. Ramsey, *Experiments with separated oscillatory fields and hydrogen masers*, Nobel Lecture (1989).
- [58] W. E. Lamb, and R. C. Retherford, *Fine Structure of the Hydrogen Atom by a Microwave Method*, *Physical Review* **72**, 241–243 (1947).

